Stress Estimation for Well 16A(78)-32 Based on Sonic Logging Data Using Machine Learning Model Trained to Laboratory Triaxial Ultrasonic Velocity Data

Report documenting completion of Milestone 2.3.1 of Utah FORGE Project 2439: A Multi-Component Approach to Characterizing In-Situ Stress at the U.S. DOE FORGE EGS Site: Laboratory, Modeling and Field Measurement

Ayyaz Mustafa[a], Andrew Bunger[a,b,*] Mark Kelley[c]

a Department of Civil and Environmental Engineering, University of Pittsburgh, Pittsburgh, PA, USA

b Department of Chemical and Petroleum Engineering, University of Pittsburgh, Pittsburgh, PA, USA

c Battelle Memorial Institute, Columbus, OH, USA

*Corresponding author: bunger@pitt.edu

Last Updated: 25 September 2023

Table of Contents

List of Figures

List of Tables

1. Technical Summary

Three optimized machine learning (ML) predictive models were employed for the prediction of in-situ stresses including vertical, minimum horizontal and maximum horizontal stresses in Utah FORGE well 16A(78)-32 using field sonic log data. Firstly, the ML models were trained and tested using laboratory-based triaxial ultrasonic wave velocity (labTUV) data wherein wave velocities were measured with various combinations of true triaxial applied stress. The labTUV data represent the Granitoid formation retrieved from well 16A(78)-32. The labTUV data include compressional, fast shear, and slow shear velocities in each of three directions for a total of nine velocities for each stress combination. The ultimate objective of this work is to predict the in-situ stresses using field sonic log data which are measured in the vertical direction. Therefore, only the vertically-propagating compressional and shear wave velocities were utilized to develop ML models. The algorithms of trained ML models were then employed for the estimation of in-situ stresses through interpreting field sonic logs. Also, because vertical (overburden) is often well constrained, one approach explored here is to take the vertical stress also as known and train the model to predict the two horizontal stresses.

The work has been divided into two folds. Firstly, the feed forward artificial neural network (FFNN) technique was applied to develop three data-driven ML predictive models for vertical and two orthogonally oriented horizontal stresses in the Granitoid formation using labTUV data. The first ML model was trained for vertical stress 'σ_z' using labTUV dataset using vertically propagating compressional, fast shear, and slow shear wave slowness as input features. The second and third ML models were developed for horizontal stress in x and y-directions ('σ_x' and 'σ_y') using labTUV dataset using compressional, fast shear, slow shear wave slowness, and stress in vertical direction as input features. The models were trained using seventy percent (70%) of the data points while testing and validation of models was further performed on fifteen percent (15%) of the data points. The prediction performances of ML models were evaluated using residual errors, root mean squared error (RMSE), average absolute percentage error, and determination coefficient (R^2). The optimum settings (neuron structure and hyperparameters) of trained ML models were then implemented to predict the in-situ vertical and horizontal stresses in the geothermal well 16A(78)-32 using field sonic log and vertical stress (field estimation) data. Prior to the execution of FFNN algorithm, the available data were thoroughly explored and analyzed through different exploratory data analysis (EDA) techniques in order to understand the data distribution, trends, patterns, interrelationship of input and output features, and to identify the relative importance of input features with respect to output.

Open source software, namely *Python (ver:3.9.13)*, was used for the EDA analyses. Various libraries of *Python (ver:3.9.13)* include *Pandas, Seaborn, Matplotlib*, and *SciPy Pandas, Seaborn, Matplotlib,* and *SciPy*. The codes and algorithms were executed using two on two different integrated development environments (IDEs) such as *Spyder (ver:5.2.2)* and *Visual Studio Code (ver: 1.81.1.)*. EDA such as statistical parameters, histograms, correlation coefficients using Pearson, Spearman, and Kendall criteria, violin plots, heat maps, and pair plots, and so forth is applied prior to the ML model execution. While reflective of the chosen testing matrix rather than intrinsic rock properties, such a routine of quantifying descriptive statistics is nonetheless a part of good practice as it aids with selection of ML models and training strategies that are suited to the nature of the datasets.

The ML modelling was performed using the FFNN algorithm executed using *Deep Learning Toolbox* of *MATLAB 2022* software. ML models were optimized by tuning different hyperparameters such as neuron count in hidden layers, training function, activation function, and realization count in order to finally achieve reliable and consistent prediction outcomes. Furthermore, the optimized FFNN models were generalized through sensitivity analysis to uncover the underlying physics. Sensitivity analysis revealed the impact of each input feature on target output (stress) following the underlying physics of the ML models. In the second phase, optimized ML models were employed on field sonic logs (blind dataset) for the prediction of in-situ stresses. As the models were trained on an experimental dataset representing the core samples retrieved from the depths of 5474 and 5850 feet, a log interval ranging from 5000 to 6000 feet was

selected for in-situ stress prediction using trained ML models. The empirical mathematical correlations were also extracted from the optimized ML models that can be applied to estimate vertical and horizontal stresses in the Granitoid formation provided that the same ranges of input and output features are used.

All three ML models demonstrated consistent and reliable prediction performance for the vertical and two horizontal stresses in terms of low average absolute percentage error (AAPE), root means squared error (RMSE) and high coefficient of determination (R^2). The first ML model for laboratory-based vertical stress (σ_z) exhibited the training (model building) and testing (validation) RMSE of 1.7 and 1.65, and AAPE of 2.51 and 2.47, respectively. For the 'σ_z' stress, R^2 was found to be 0.954 and 0.963 for training and testing and validation dataset, respectively. Further, the model also exhibited excellent performance on log data (blind dataset) for in-situ vertical stress prediction. The log-based ML predicted field vertical stress (S_v) was found to be in good agreement with field estimation of stress reflecting RMSE of 0.66 and 1.5, and AAPE of 1.58 and 3.36, for the depths of 5474 and 5850 feet, respectively.

Secondly, for the first laboratory-based horizontal stress 'σ_x' model, the R^2 values were observed to be 0.984 and 0.971 for the testing and validation and training results. The excellent model functioning was reflected by the low RMSE and AAPE errors for testing (1.48 and 3.1) and training (2.05 and 3.03) prediction, respectively. This model was employed for the prediction of maximum horizontal stress (SH_{max}) in the field using the same input features for which the model was originally trained, however, in this case input features were obtained from the field sonic logs and vertical stress data. The predicted stress was found to be in harmony with field estimation of SH_{max} stress. The predicted SH_{max} exhibited RMSE and AAPE of 0.9 and 0.05 at the depth of 5474 ft and 2.89 and 0.15 at the depth of 5850 ft, respectively. Likewise, the second laboratory-based horizontal stress model for 'σ_y' demonstrated the R^2 value of 0.986 for testing and 0.955 for training prediction. The prediction RMSE and AAPE were observed to be 1.41 and 2.50, and 0.61 and 1.1 for testing and validation and training datasets, respectively. This model was employed for the prediction of minimum horizontal stress (SH_{min}) in the field using sonic logs and vertical stress. The predicted SH_{max} reflected excellent accuracy when compared to the field estimated SH_{max} with RMSE and AAPE of 2.1 and 8.05 at the depth of 5474 ft and 0.82 and 2.82 at the depth of 5850 ft, respectively.

In summary, accuracy measures revealed excellent prediction performance of all three ML models for both laboratory-based and log-based stress predictions. Sensitivity analysis revealed that the proposed ML models are able to capture the underlying physics demonstrating the variations of ultrasonic wave velocities under the influence of stress. Therefore, the trained models successfully predicted the blind sonic log data for the reliable estimation of in-situ stresses. Hence, the proposed ML models function well for both experimental and field log datasets. The ML based explicit mathematical correlations can be confidently applied for stress estimation without running the ML programs provided that the input features and ranges are the same.

2. Task and Milestone Description

This report documents the task completion and technical accomplishments comprising achievement of Milestone 2.3.1, as per the project Statement of Project Objectives (SOPO). The validation of milestone accomplishments is illustrated in Figures 14 through 18 demonstrating the key outcomes of the developed machine learning models for vertical and horizontal stresses.

Milestone 2.3.1: The task incorporates the development and implementation of ML models for the prediction of in-situ vertical (S_v), minimum horizontal (SH_{min}) and maximum horizontal (SH_{max}) stresses in well 16A(78)-32. The detailed description about the experimental work was documented in Milestone report 2.1.1 of the project.

This Milestone task 2.3.1 follows the Milestone report 2.2.1 that elaborated the ML model development and validation strategy comprehensively. In this Milestone task, prediction performances of ML models are

further improved and implemented carefully for the estimation of in-situ stresses (i.e., S_v, SH_{min}, and SH_{max} over the depth ranging from 5000 to 6000 feet in the well 16A(78)-32). A comparison between ML-based and field-based in-situ stresses estimations reflected the excellent harmony in terms of nominal errors at the sampling depths. The accomplishment of the Milestone task 2.3.1 is illustrated in Figures 20 through 22 demonstrating coherence between ML-based and field-based estimation of in-situ stresses.

Further, the ML models were capable of capturing the physical phenomenon between the sonic wave slowness and stresses (Figure 19). The underlying physics was uncovered by the sensitivity analysis (model generalization) of each input feature on the target output of the trained models which is a supporting argument for the successful implementation of ML models on the field sonic and stress datasets at the sampling depths. The sensitivity analysis revealed the impact of each input feature on the target output (stress) through a specific physical relationship.

Various stages were accomplished during the model development phase such as EDA, ML model development, uncovering the underlying model's physics, and implementation of optimized model for field stresses estimation. This report begins with a description of the ML technique FFNN used for the prediction modelling of stresses. Then, a comprehensive ML modelling workflow with each step is presented. The main findings of EDA are discussed for the given input and output features. A thorough illustration of the main features of FFNN model optimization and hyperparameter tuning are provided. Subsequently, models' accuracy and prediction performance are discussed. The sensitivity analysis was presented to check the models' ability of capturing underlying physics. Then, optimized ML models were implemented on field sonic log data for the estimation of in-situ stresses in well 16A(78)-32. The last section demonstrates the mathematical correlations development for the three FFNN prediction models. Finally, the key findings and important postulates are provided in conclusions.

3. Artificial Neural Network (ANN)

Artificial neural network (ANN) is one of the extensively employed ML methods for handling prediction issues, data mining, pattern recognition, and approximation (Mozaffari and Azad, 2014) 24, 25. Although various types of ANN techniques are used, backpropagation and feedforward ANN algorithms are the most implemented for prediction and training (Chau, 2007). ANN uses various learning functions, networks and activation functions to provide the required prediction solution for the specified problem (Mohaghegh et al. 1994).

ANN solves the underlying problem through replicating the components and operations of the nervous system of human beings. Artificial neurons are components of an explicit architectural network that are chosen based on the specifications of the given engineering challenge (Ali, 1994). In order to produce accurate, dependable, and consistent prediction outcomes, ANN establishes connections among the nonlinear variables using a massive collection of algorithms (Otchere, 2021). In general, feed-back neural networks (FBNN) and feed-forward neural networks (FFNN) are the two types of ANN that are widely used. FFNN is a basic and simplest ANN design that uses interconnected perceptron layers to build a forward-only, unidirectional process of transferring information. In order to identify a precise and pertinent output feature, the knowledge of input features is transmitted nonlinearly via activation function of hidden layers. The second variant, which has the same architectural qualities as FFNN with the extra feature of establishing a back loop, is equally accepted, and frequently used for ANN applications (Saggaf et al. 2003). The back loop feature of FBNN iteratively refines the predicted output feature by delivering error information to execute the algorithm again to modify the weights until accuracy measures (errors and correlation coefficients) can no longer be improved (Saikia, 2020).

Numerous interconnections were established through the specified routes for the interaction between the nodes of ANN structure. Each node of the hidden layer is assigned with specific weight to streamline the functionality of ANN structure (Hornik et al., 1989). During the training process, algorithms are fed with input features in the form of vectors. After the output errors are routed back, the weights between the

nodes are finely adjusted using gradient descent. The process is kept repeating until the output errors are not further improved (note: all variables appearing in equations in this report are defined in the Nomenclature section near the end of the report).

$$\Delta W(t) = \Delta W(t-1) * \alpha + \Delta E * \eta * (t) \qquad \text{(Eq. 1)}$$

The gradient descent uses the error function to update the weights between the nodes of ANN structure as shown in Eq. 1 (Avseth and Mukerji, 2002). Where η, E, Δw, and α, demonstrate adjusted weights, output error, learning components, and momentum, respectively.

There are various advantages of using ANN as compared to other supervised ML algorithms.
1. It has the ability to handle the non-linearity and complexity association between input and output features.
2. ANN functions with great efficiency while dealing with high dimensionality of the data.
3. ANN can demonstrate the complicated classification groups and non-limiting functions that contain output and input features.

4. Methodology – Modelling Approach

4.1. Machine Learning Modelling Workflow

The ML workflow started with data collection, data cleaning and exploratory data analysis of experimental dataset to explore the data distribution, patterns, relationships, and relative importance of input features with respect to output features. Exploratory data analysis was performed using different libraries of open-source software *Python (ver:3.9.13)* (Python software foundation, 2023) and program codes were executed on two integrated development environments (IDE) including *Spyder (ver:5.2.2)* (Cerezo et al. 2023) and *Visual Studio Code* (Microsoft,2015). The *Pandas (ver:1.4.4)* library of *Python* (McKinney, 2022) was used to extract the *Microsoft Excel* data and generate a data frame on *Python* software. The *Seaborn (ver:0.11.2)* library was employed for generating the heat maps, pair plots, histogram, kernel density estimation (KDE) function , and violin plots (Waskom and Seaborn, 2023). All EDA plots were generated using the *Matplotlib.pyplot* module of *Matplotlib (ver:3.5.2)* library of *Python (ver:3.9.13)* software (Hunter and Droettboom, 2016). Statistical features and correlation coefficients (Pearson, Spearman, and Kendall) were determined using *Scipy (ver:1.9.1)* library (Jones et al. 2023). After EDA analysis, the dataset is ready to be fed for ML modelling. All the Python libraries and IDE (Integrated Development Environment) collectively function under the *Anaconda (ver:22.9.0)* package (Anaconda Inc. 2023).

Subsequently, the FFNN type of ANN technique with the feature of back propagation was employed to develop prediction models for vertical and horizontal stresses in the Granitoid formation. After that, the trained models were implemented to estimate in-situ stresses in well a6A(78)-32 using field sonic log data. Training of the model was performed using the *Deep Learning Toolbox* of MATLAB software (MATLAB, 2022). Grid search cross validation process was used for optimizing the hyperparameters in FFNN. The optimized FFNN models were used for stress estimation using field sonic log data. The complete workflow adopted in this study is shown in Figure 1.

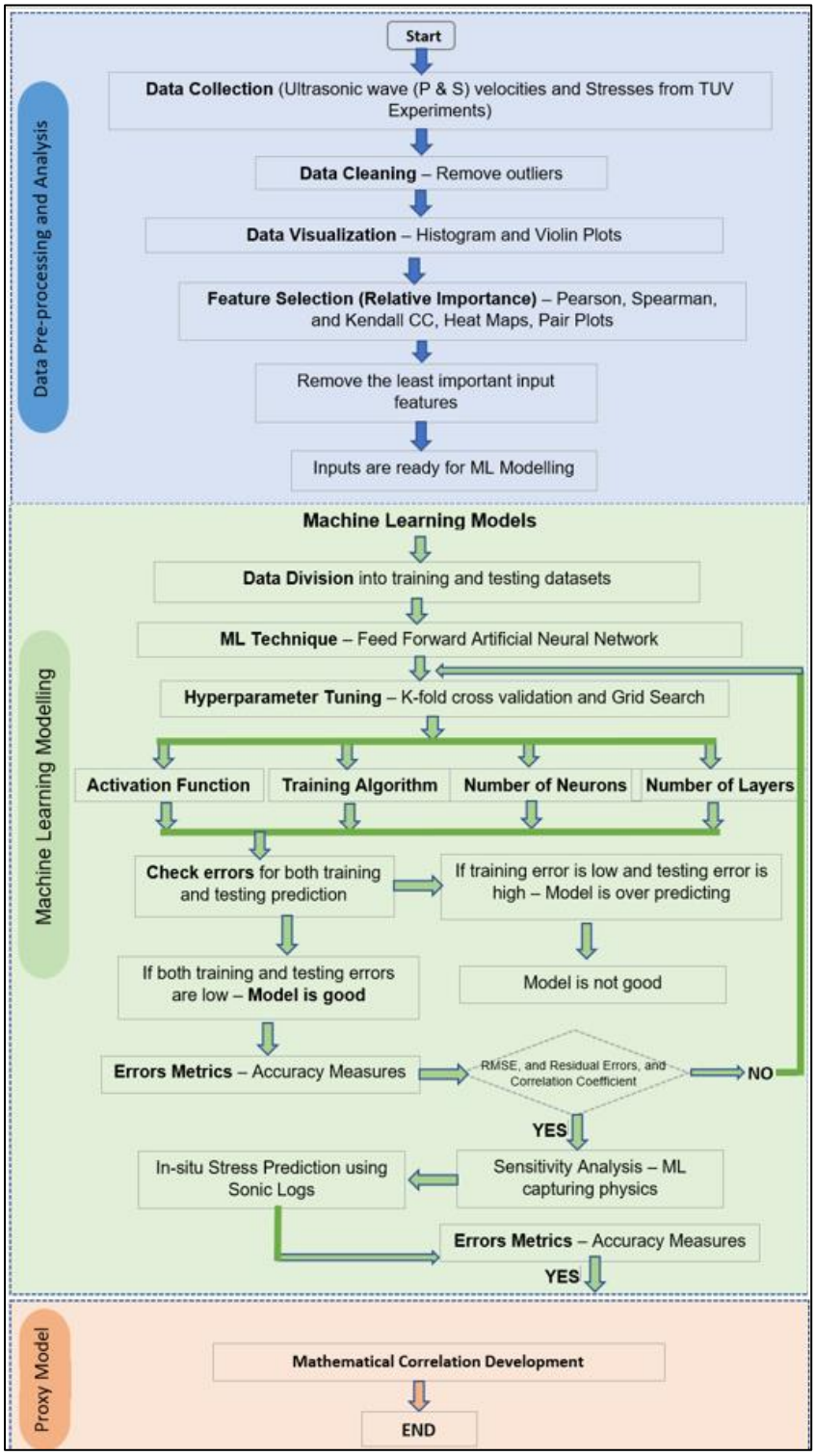

Figure 1: Modelling Workflow for this study

4.2. Exploratory Data Analysis (EDA)

In this study, ultrasonic wave velocity (actually the inverse of the velocities, the P- and S-wave slowness) and stress data were used to develop three ML prediction models for vertical stress (σ_z) and two orthogonally oriented horizontal stresses (σ_x and σ_y). The ML models were trained on labTUV datasets representing the Granitoid formation with samples retrieved from 5474 ft MD and 5850 ft MD,

respectively. Further description of labTUV experiments can be found in Bunger et al. (2023). Then, optimized algorithms of trained models were employed to predict the in-situ stresses using field sonic logs. The in-situ stresses were predicted for the depth interval ranging from 5000 to 6000 ft in well 16A(78)-32.

Based on this available dataset, initially 46 data points were available. However, after the data cleaning, a total of 41 TUV data points were utilized that contain P-wave (h_{zz}), and S-wave slowness (h_{zy} and h_{zx}), in the z-direction under different combinations of applied stresses 'σ_z', 'σ_x', and 'σ_y' in z, x, and y directions, respectively (Table 1). Note that throughout this report, each loading combination is designated an identifier, its "dataset number". While the order of these does not have physical meaning, it is nonetheless sometimes useful for visualizing the span of the data to report data by this number. Each point of dataset represents the result of one labTUV experiment.

Table 1: Experimental dataset used for ML predictive modeling.

Experiment No.	h_{zz} **(μs/ft)**	h_{zy} **(μs/ft)**	h_{zx} **(μs/ft)**	σ_z **(MPa)**	σ_x **(MPa)**	σ_y **(MPa)**
1	54.96	107.75	105.12	19.80	19.89	19.75
2	56.16	108.10	103.34	29.89	29.89	29.89
3	55.20	108.07	103.96	40.08	29.89	29.99
4	55.20	108.27	103.49	39.98	29.89	39.84
5	53.76	106.66	104.16	49.69	29.89	39.98
6	54.00	106.97	103.30	49.93	39.79	39.98
7	54.58	108.26	103.37	49.93	40.03	29.99
8	55.20	107.35	103.34	49.93	39.88	25.11
9	53.04	105.49	103.23	49.93	40.03	34.86
10	53.76	105.15	103.23	49.93	39.88	37.50
11	54.72	106.18	103.80	49.93	40.13	32.38
12	54.48	105.66	103.23	49.93	40.13	31.06
13	53.28	104.76	103.71	49.93	49.78	31.06
14	54.58	105.62	103.94	49.93	45.20	31.06
15	55.04	106.48	103.12	49.93	55.00	31.06
16	53.76	104.54	103.64	49.93	59.92	31.06
17	54.72	105.65	105.22	49.93	65.00	31.06
18	54.50	105.06	104.38	49.93	62.46	31.06
19	52.99	103.75	103.58	49.93	62.46	31.06
20	53.62	104.01	103.61	49.93	64.02	31.06
21	53.95	104.29	103.36	54.85	62.46	31.06

Experiment No.	h_{zz} (μs/ft)	h_{zy} (μs/ft)	h_{zx} (μs/ft)	σ_z (MPa)	σ_x (MPa)	σ_y (MPa)
22	53.76	104.81	102.97	45.00	62.46	31.06
23	55.06	105.50	102.21	47.44	62.46	31.06
24	53.28	104.14	102.72	52.51	62.46	31.06
25	54.24	94.71	100.85	19.94	19.89	19.70
26	53.76	92.79	100.71	30.38	30.04	29.74
27	55.68	94.27	101.81	40.08	39.84	39.74
28	62.72	94.27	100.22	50.42	29.94	39.98
29	55.89	94.05	99.90	49.69	40.03	39.88
30	67.68	96.08	100.60	40.23	29.89	40.13
31	53.76	92.28	100.37	40.08	29.89	49.98
32	54.48	93.81	99.72	50.17	30.28	49.98
33	53.76	92.12	101.56	43.98	39.69	39.88
34	54.72	92.55	101.03	46.91	40.03	39.88
35	54.24	92.38	100.57	48.51	40.03	40.13
36	55.44	93.60	101.17	49.93	40.03	40.13
37	55.68	93.82	94.19	42.08	39.88	40.13
38	55.68	94.24	100.54	54.85	40.13	40.23
39	55.44	93.60	94.23	45.15	40.03	49.88
40	54.24	92.80	99.51	45.10	40.03	55.10
41	54.24	92.88	101.80	45.05	35.30	50.12

Note that throughout this report, slowness ('h') is given two subscripts, where the first gives the propagation direction and the second gives the direction of particle motion. Hence, 'h_{zz},', 'h_{zy}', and 'h_{zx}' all describe waves propagating in the z-direction and indicate the P-wave, the y-polarized S-wave, and the x-polarized S-wave, respectively. The illustration of waves propagation direction and particle movement is provided in Figure 2.

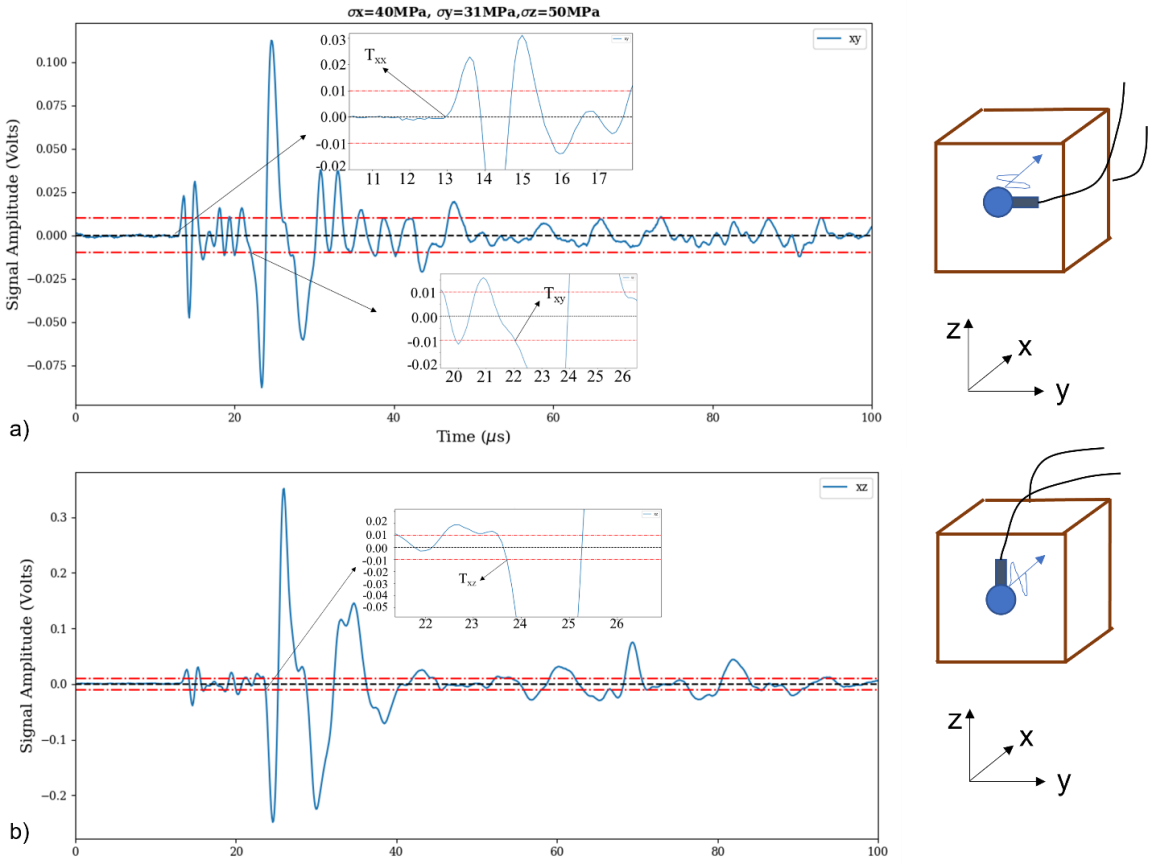

Figure 2: Example of waveforms from Lower Granitoid, x-direction. Waveforms result from two separate experiments with transducers oriented to capture the y-polarization (top) and z-polarization (bottom). Sketches show sample and transducer orientation to illustrate propagation direction and shear wave polarity for each of these cases. (Bunger et al. 2023).

The first ML model was trained to predict the vertical stress 'σ_z' using P and S-wave slowness 'h_{zz},', 'h_{zy}', and 'h_{zx}' as input features. This model was employed to predict the vertical stress (S_v) in well 16A(78)-32. The second ML model was developed using four input features including 'h_{zz},', 'h_{zy}', 'h_{zx}' and 'σ_z' to predict the horizontal stress 'σ_x' applied in x-direction. The 'σ_x' stress model was used to predict the SH_{max} in well 16A(78)-32 using sonic logs and vertical stress.

The model developed for the second horizontal stress 'σ_y' applied in the y-direction was implemented to predict the SH_{min} for the same well. For this model, the same four input features ('h_{zz},', 'h_{zy}', 'h_{zx}' and 'σ_z') were utilized. During the development phase, labTUV datasets were split into three portions. The first portion (seventy percent) of the dataset was dedicated for model training while validation and testing of the trained model was performed using the second (15%) and third (15%) portions of the data points. The entire dataset is shown in Figure 3. Testing and training sets of data used for 'σ_z', 'σ_x', and 'σ_y' prediction models are presented in Figures 4 through 6, respectively.

Testing and training datasets were firstly subjected to EDA for the purpose of data cleaning, understanding the data distribution, trends, patterns, relative importance, and relationships of input and output features. The EDA is essential for feature selection prior to the execution of ML algorithms to ultimately generate a robust prediction model. Important statistical parameters such as maximum, minimum, mode, mean, median, kurtosis, skewness, and standard deviation of input and output features

are demonstrated in Table 2. The statistical indicators are reflective of the choices of testing matrix (load combinations) carried out in the lab, not of any intrinsic rock behavior. Visualization of data distribution for each feature is provided by the violin plots that expresses the data points in the form of a KDE function. Violin plots are important to visualize the extreme values, inter quartile range (IQR), and arithmetic mean in the dataset as shown in Figure 5. Bimodal distribution of data can also be easily identified by visualizing violin plots as shown for 'h_{zy}' and 'σ_x' features (Figure 7).

Further, boxen plots are another visualization tool that are essential to exhibit the median, IQR, and extreme values (Figure 8). The cluster maps demonstrated the cluster connections on the basis of collinearity between the pairs of input and output features as shown in Figure 9. Cluster maps were generated using the Spearman, Pearson, and Kendall correlation criteria. The patterns, trends and similarities/differences between the datasets have been illustrated using swarm plots (Figure 10).

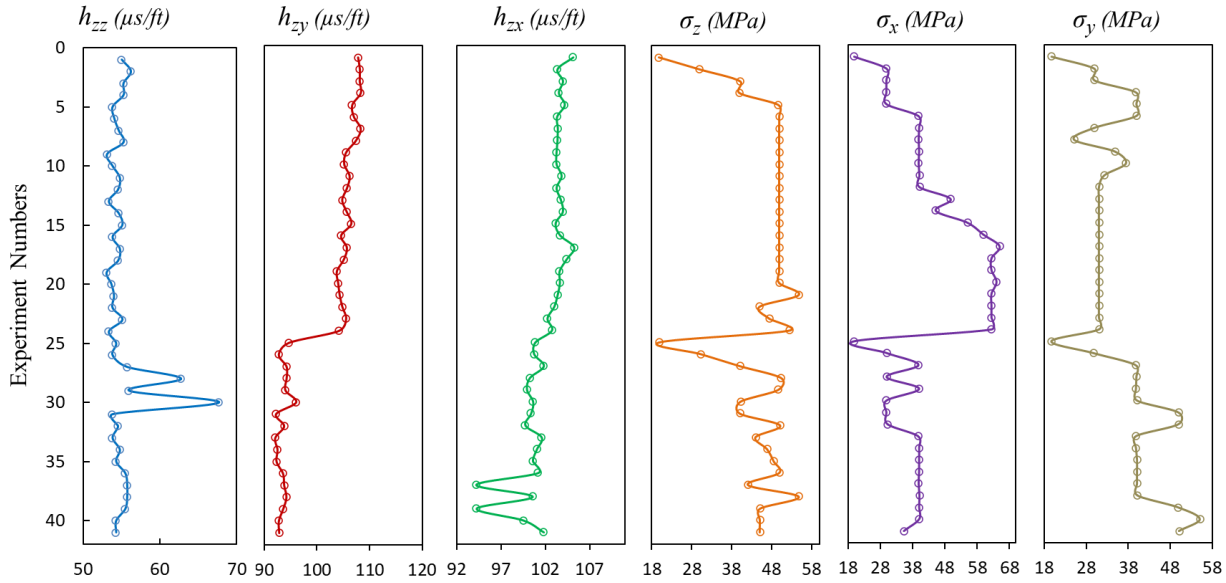

Figure 3: Total Dataset used for all three ML prediction models.

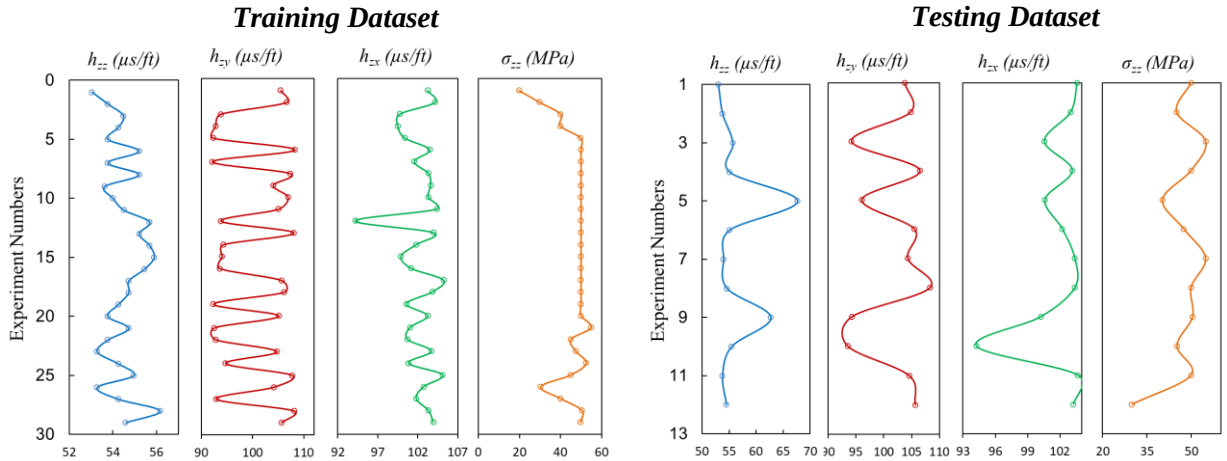

Figure 4: Training and testing dataset used for vertical stress 'σ_z' prediction model.

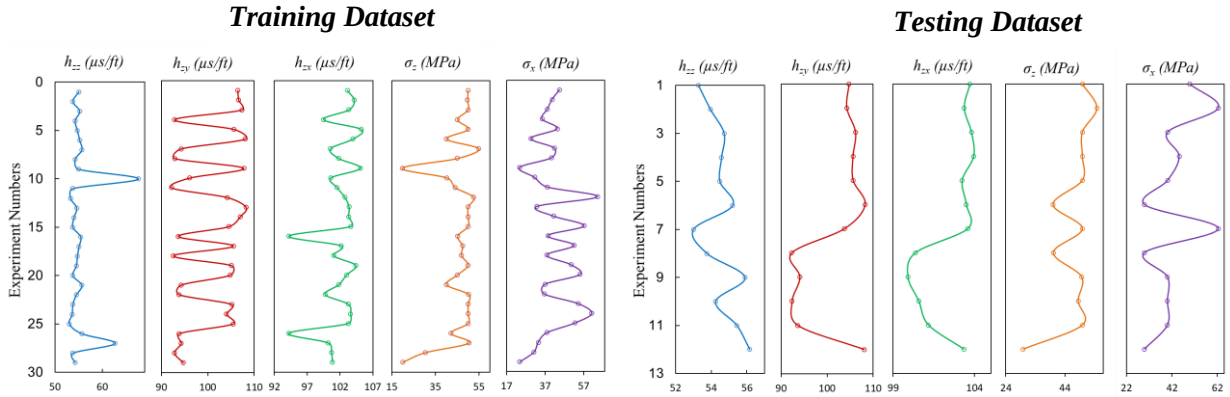

Figure 5: Training and testing dataset used for horizontal stress 'σ_x' prediction model.

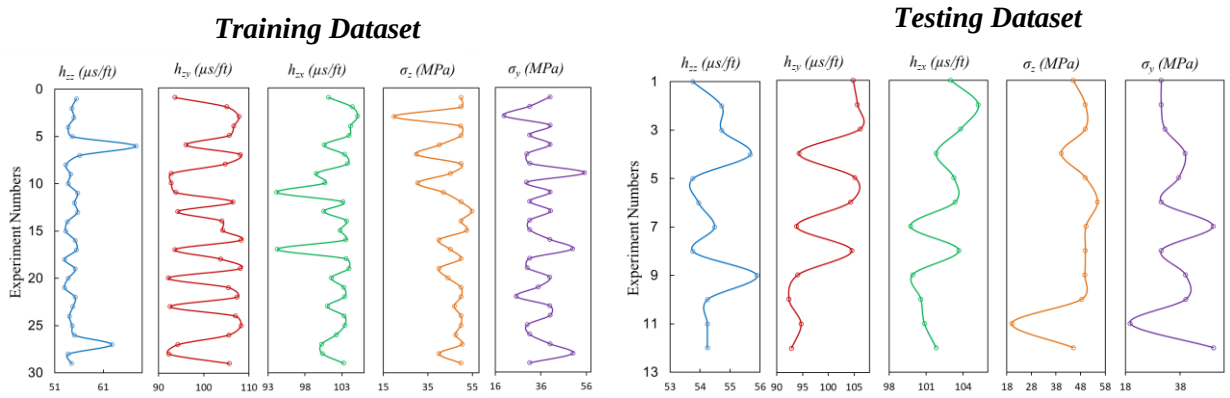

Figure 6: Training and testing dataset used for horizontal stress 'σ_y' prediction model.

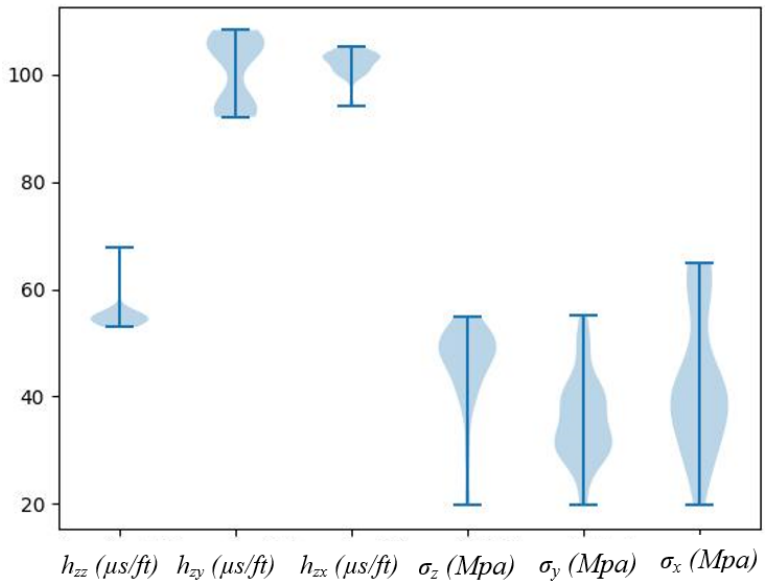

Figure 7: Violin plots for input and output variables

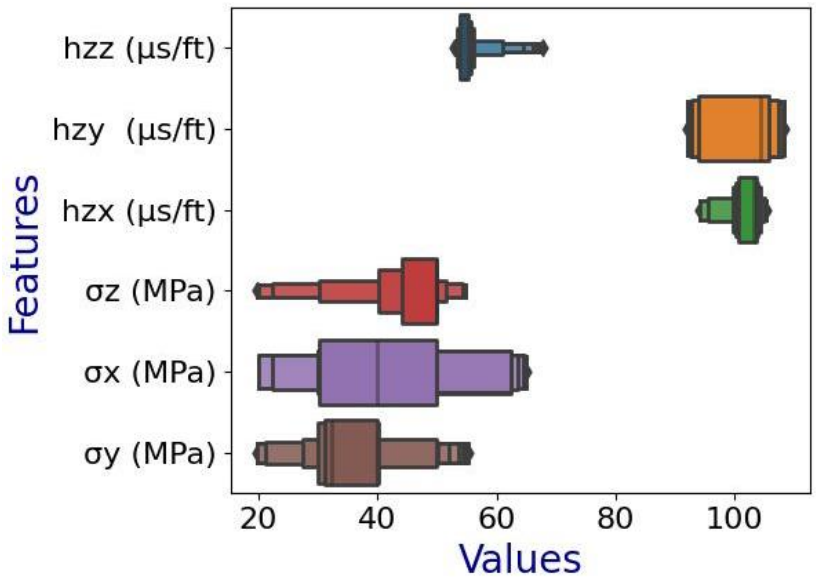

Figure 8: Boxen plots for input and output features.

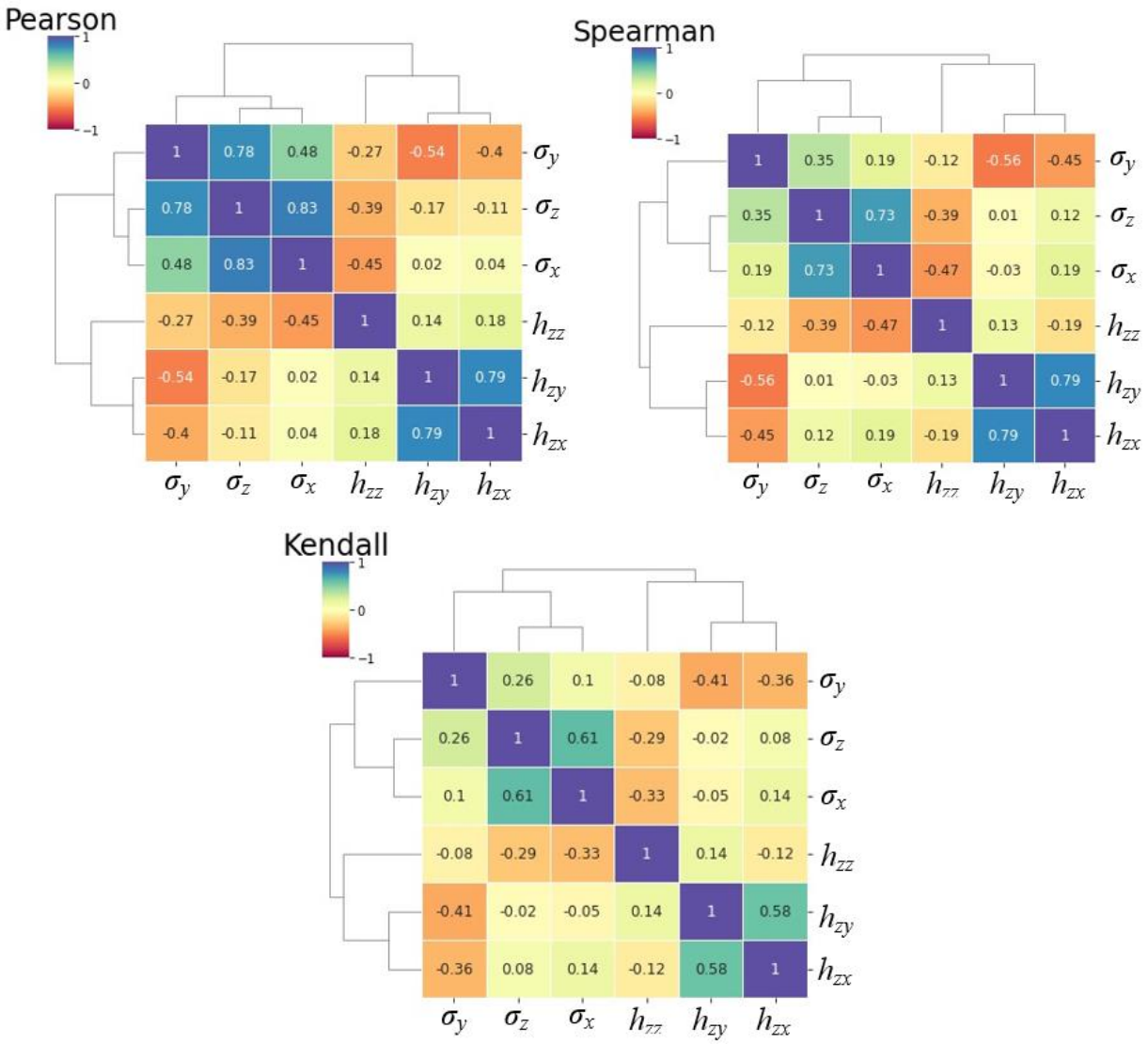

Figure 9: Cluster maps of features using the Pearson, Spearman and Kendall criteria.

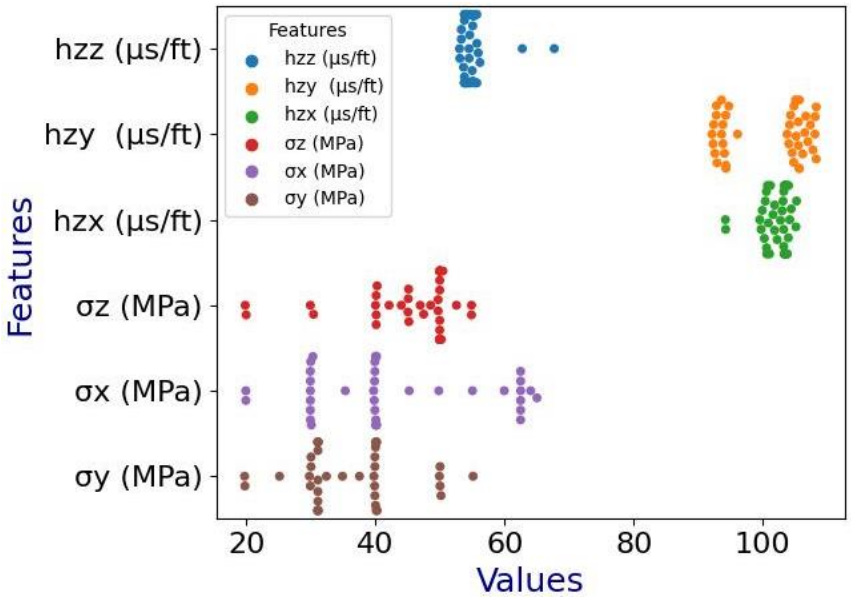

Figure 10: Swarm plots of input and output features.

The relative importance of all the input features was explored using three criteria namely Pearson, Spearman, and Kendall correlation coefficients (R) as shown in Figure 11. For the first ML model, the input feature 'h_{zz}' exhibited strong inverse correlation with output 'σ_z' while relatively weaker correlations were observed for the other two input features 'h_{zy} 'and 'h_{zx}'. On the other hand, horizontal stress 'σ_x' exhibited a strong direct and inverse relationship with vertical stress 'σ_z' and P-wave slowness 'h_{zz}', respectively. S-wave slowness 'h_{zy}' and 'h_{zx}' demonstrated relatively weaker correlation with 'σ_x'. For the case of other horizontal stress 'σ_y', two input features 'h_{zy}' and 'h_{zx}' demonstrated a strong inverse relationship while 'σ_z', and 'h_{zz}' reflected a weaker direct relationship with 'σ_y'. Pearson, Spearman, and Kendall's correlation criteria are provided in Eqs. 2 through 4, respectively.

Furthermore, pair plots among all input and output variables demonstrated the inter-relationships between all pairs of output and input features in a single plot (Figure 12). The velocity variations with stresses are prominent for the Granitoid formation. It could be observed in the pair plots that P- and S-wave slowness have inverse and direct relationships with 'σ_z' respectively. The horizontal stress 'σ_x' exhibited almost similar relationship trends with 'h_{zz}', 'h_{zx}' and 'h_{zy}'. However, relationship trends are reverse for 'σ_z'. The diagonal of the pair plot represents the histograms with KDE distribution of each feature. P-wave slowness exhibited an inverse relationship with S-wave slowness.

Histograms shown within pair plots revealed that P-wave slowness 'h_{zz}' is positively (right) skewed indicating that most of the data points are clustered towards the left side of distribution reflecting non-symmetric distribution. A major portion of the 'h_{zz}' dataset is clustered towards the left side of the plot (values are lower than the mean values) that leads to the longer tail on right side of the distribution. The S-wave slowness 'h_{zx}' and 'h_{zy}' is not skewed or slightly negatively skewed indicating fairly symmetric distribution of data on both sides of the mean value. The majority of data points exist around the mean values of these input features. On the contrary, the stresses 'σ_z', 'σ_x', and 'σ_y' data are negatively (left) skewed exhibiting that the majority of the dataset is larger than the mean value with a longer tail on the left side. The distribution revealed that the mean value is smaller than mode and median. Kurtosis of P-wave slowness is leptokurtic with heavier tailed and peaked distribution as reflected by a higher positive value. Most of the data points lie in the tail of distribution instead of in close proximity of the mean value. Other

five input features such as S-wave slowness (h_{zx} and h_{zy}) and stress (σ_z, σ_x, and σ_y) data distribution reflect platykurtic distribution with lower and broader peaks. The tail of data distribution curve is lighter than normal distribution indicating minimum chances of outlier existence in the dataset. These features are lacking extreme values with flatter distribution around the mean value that reflects good quality of data.

$$\rho_{pearson} = \frac{k\sum ab - (\sum a)(\sum b)}{\sqrt{k(\sum a^2) - (\sum a)^2}\sqrt{k(\sum b^2) - (\sum b)^2}} \quad \text{(Eq. 2)}$$

Where b and a represent the respective variables, and number of samples are represented by k.

$$\rho_{spearman} = \rho_{pearson}\frac{\mathrm{cov}(a,b)}{\gamma_a \gamma_b} \quad \text{(Eq. 3)}$$

$$\tau_{kendall} = \frac{n_c - n_d}{n(n-1)/2} \quad \text{(Eq. 4)}$$

Where n_c and n_d represent the values of number of concordant and discordant pairs and total number of samples are represented by 'n'.

Table 2: Statistical indicators of dataset used in ML Modelling

Statistical Parameters	h_{zz} *(µs/ft)*	h_{zy} *(µs/ft)*	h_{zx} *(µs/ft)*	σ_z *(MPa)*	σ_x *(MPa)*	σ_y *(MPa)*
Minimum	53.0	92.1	94.2	19.8	19.9	19.7
Maximum	67.7	108.3	105.2	54.9	65.0	55.1
Mean	55.0	100.8	102.1	45.6	42.4	35.8
Mode	54.7	93.6	103.2	49.9	40.0	31.1
Median	54.5	104.3	103.1	49.9	40.0	32.4
St. Dev.	2.5	6.3	2.4	8.0	12.7	7.9
Kurtosis	17.5	-1.8	4.2	3.9	-0.7	0.2
Skewness	4.0	-0.3	-1.8	-2.0	0.5	0.4

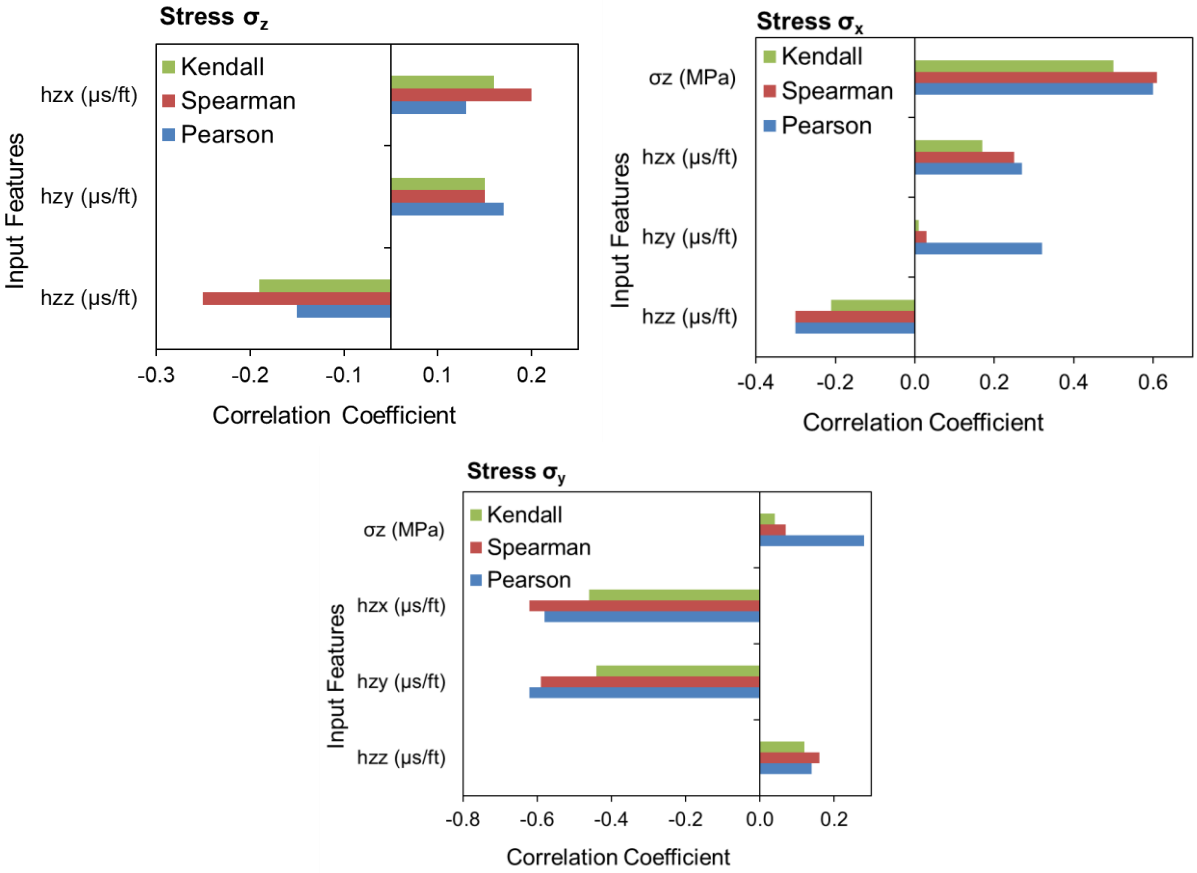

Figure 11: Coefficient of correlations of input variables with output showing relative importance.

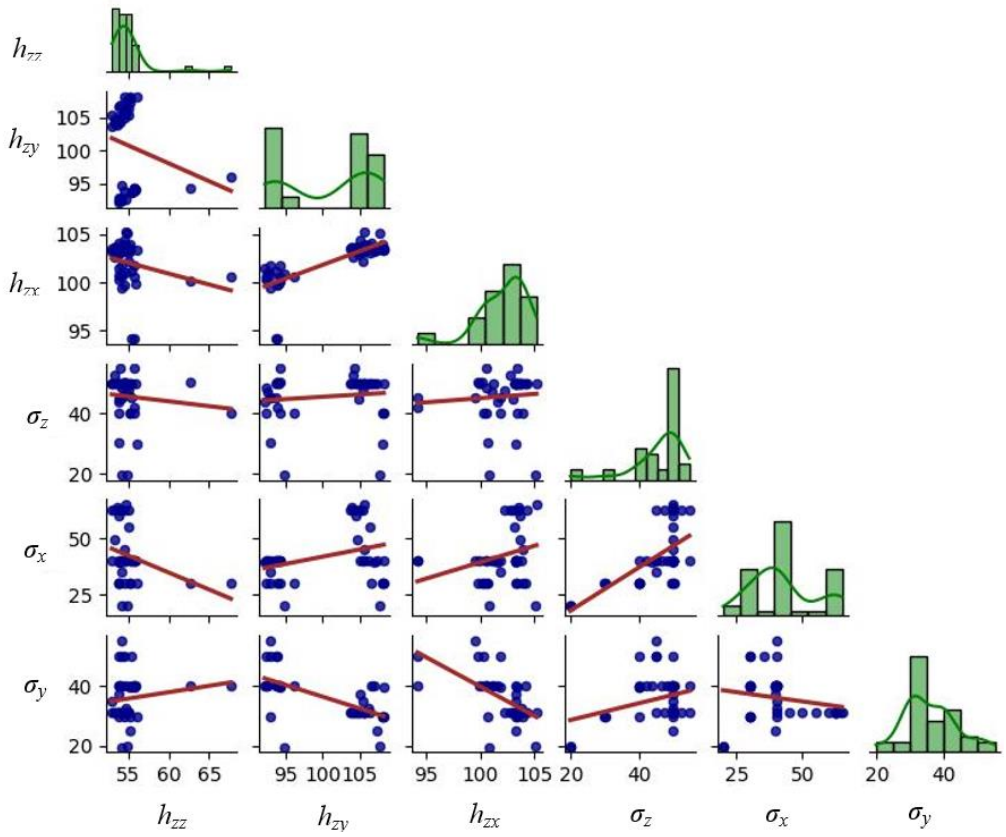

Figure 12: Pair plots showing cross plots between input and output features.

4.3. Hyperparameter Tuning and Models Optimization

The first stage of the study presented three robust ML models developed to predict the stresses in vertical (σ_z) and two horizontal directions (σ_x and σ_y) for the Granitoid formation using fully connected FFNN techniques with the additional feature of back propagation. The ML model was trained using ultrasonic wave velocities in the z direction that were obtained from the labTUV experiments.

The FFNN prediction model for stresses was optimized by improving the coefficient of determination (R^2) and minimizing the prediction errors through different strategies of hyperparameter tuning. The data points were split into two halves. The train test split function in the *MATLAB* software (MATLAB, 2022) was used to divide the data. The data splitting was an arbitrary occurrence and was done in such a way that testing and validation data contained the range of the input variables present in the training dataset. Seventy percent of the dataset was set aside for the model training and the remaining thirty percent was set aside for testing (15%) and validation (15%). Seed function was used to regulate the random number generation for each run. ANN algorithm was run several times using numerous selected hyperparameters such as input features, neuron count in hidden layers, training functions, activation functions, and realizations count. The k-fold cross validation strategy was adopted during the training process in order to avoid the data overfitting.

For all three stress prediction models, the FFNN algorithm was executed for different training functions such as resilient propagation, Levenberg-Marquardt, BFGS Quasi-Newton, Scaled Conjugate Gradient, and Fletcher-Powell Conjugate Gradient to optimize the prediction accuracy (MATLAB, 2022). Best prediction results were obtained with Levenberg-Marquardt training function for stresses σ_z, σ_x, and σ_y. The best activation function was found to be Tangent sigmoidal and linear functions that connect the hidden and input layers, and the output and hidden layers, respectively, after executing the model using different activation functions such as tangent sigmoidal, logarithmic sigmoidal, soft max, linear, triangular basis activation functions (MATLAB, 2022). Optimization of neuron count in hidden layers was performed by executing the model algorithm at various neuron counts from 5 to 40 starts from lower numbers to higher (Opper and Haussler, 1996). A comparison of model performance at different number of neurons is demonstrated in Figure 13. The model accuracy was further improved by executing the model for 1000 realizations for the selected neurons count in the central hidden layer to catch the non-distinctiveness of the data points (Zhang, 2022). The optimum prediction results were achieved at 38, 14, and 10 number of neurons and 70, 68, and 6 realizations for stresses σ_z, σ_x, and σ_y, respectively, exhibiting minimum prediction errors and maximum coefficient of determination (R^2). The model performance of 100 realizations and best selected realization for the optimized neuron count are shown in Figure 14. After optimizing the neuron count and realization, the FFNN algorithm was executed at the optimum neuron structure and hyperparameters to observe the best model performances for stresses 'σ_z', 'σ_x', and 'σ_y'.

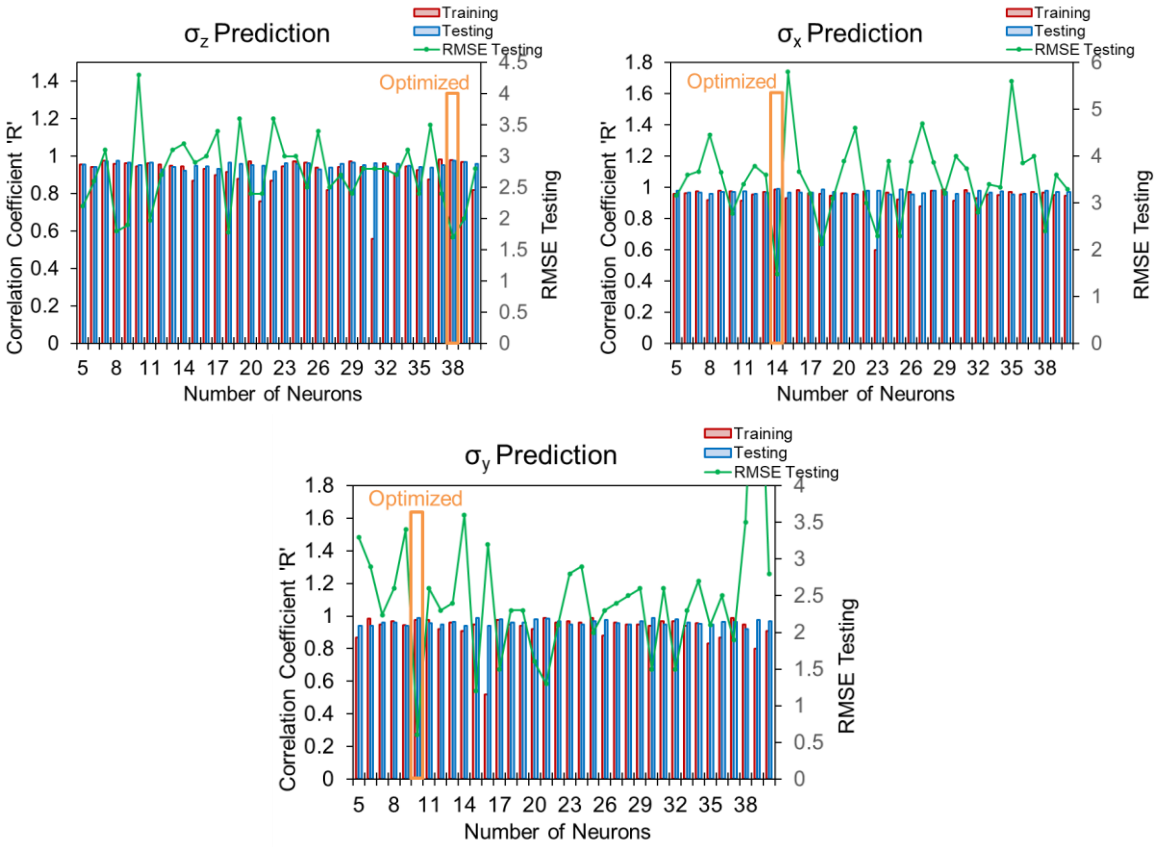

Figure 13: Neuron optimization based on prediction performance.

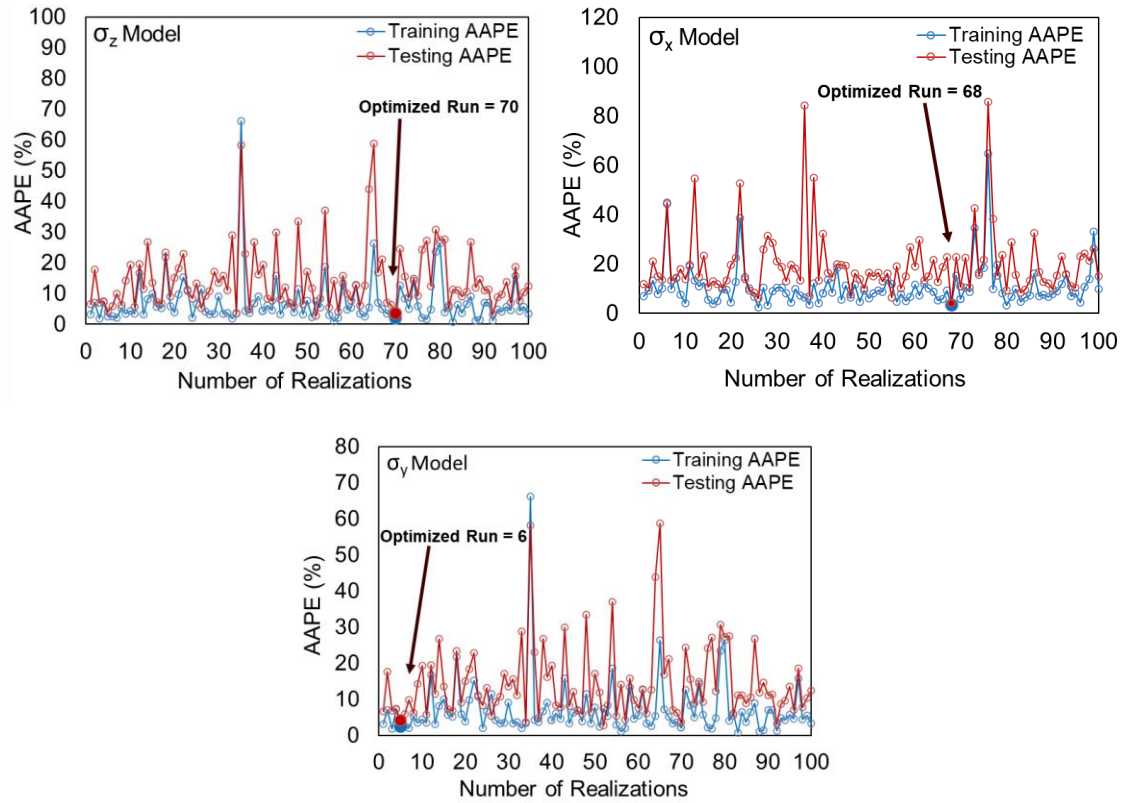

Figure 14: Prediction AAPE for selected 100 realizations at optimized neurons count for ‘σz’, ‘σx’, and ‘σy’ models.

4.4. Performance Measures

The predictive models' performances were assessed using four accuracy measures including coefficient of determination (R^2), residual errors (RE), root mean squared error (RMSE), and average absolute percentage error (AAPE). The extent of accuracy was assessed from 'R' value between predicted and actual values.

$$\text{Residual Error} = \left(\sigma_{\text{measured}} - \sigma_{\text{predicted}}\right) \quad \text{(Eq. 5)}$$

$$\text{AAPE (\%)} = \frac{\sum\left|\left(\sigma_{\text{measured}} - \sigma_{\text{predicted}}\right)\right| \frac{100}{\sigma_{\text{measured}}}}{\text{total data points}} \quad \text{(Eq. 6)}$$

$$\text{RMSE} = \sqrt{\frac{\sum\left(\sigma_{measured} - \sigma_{predicted}\right)^2}{total\ data\ points}} \quad \text{(Eq. 7)}$$

$$R^2 = \left[\frac{k\sum xy - (\sum x)(\sum y)}{\sqrt{(k(\sum x^2) - (\sum x^2))}\sqrt{k(\sum y^2) - (\sum y^2)}}\right]^2 \quad \text{(Eq. 8)}$$

The mathematical expressions of the accuracy measures are demonstrated in Eqs. 5 through 8.

5. Modelling Results

All three stress prediction models exhibited excellent performance in terms of low prediction errors and high R^2. The general topology of neuron structures for the prediction models are shown in Figure 15.

The developed FFNN models provided reliable and robust predicted vertical and horizontal stress values. The prediction performance of all three models FFNN in terms of cross plots between predicted and experimental stress values are demonstrated in Figure 16. For the vertical stress 'σ_z' prediction model, the R^2 values between predicted and experimentally determined stresses were observed to be 0.963 and 0.954 for testing (unseen data) and training (model building) datasets, respectively. The model demonstrated excellent outcome with prediction RMSE of 1.65 and 1.7, and AAPE of 2.51 and 2.47 for testing and training prediction, respectively. The FFNN training and testing predictions of all three prediction models ('σ_z', 'σ_x', and 'σ_y') are also compared with experimental stress values demonstrating good agreement between them. For the horizontal stress 'σ_x' prediction model, the R^2 values between predicted and experimental data points were determined to be 0.984 and 0.971 for testing and training data points, respectively. The excellent model functioning was reflected by the low RMSE and AAPE errors for testing (1.48 and 3.1) and training (2.05 and 3.03) prediction, respectively.

The second horizontal stress 'σ_y' prediction model also resulted in reliable and steadfast predicted values of stress with demonstration of R^2 of 0.986 for testing and 0.955 for training prediction results. The prediction error AAPE and RMSE for the stress 'σ_y' was observed to be 0.61 and 1.1 for testing and 1.42 and 2.50 for training data points, respectively, demonstrating the accuracy of model prediction. Hence, all three FFNN models for vertical and horizontal stress prediction demonstrated accurate, reliable, and consistent prediction abilities as reflected by the excellent accuracy measures. The performances for testing and validation at the optimal parameters of FFNN model in terms of mean squared error (MSE) are demonstrated in the Figure 15. The prediction performance of all three models FFNN ML model in terms of cross plots between predicted and experimental stress values and residual errors of training and testing of models are demonstrated in Figure 17.

Consequently, accuracy indicators revealed that developed three FFNN models can provide the reliable, robust and consistent prediction solution for vertical stress 'σ_z' as a function of 'h_{zz}', 'h_{zx}' and 'h_{zy}' and two horizontal stresses (mutually perpendicular) as a function of 'h_{zz}', 'h_{zx}', 'h_{zy}' and 'σ_z' for the given input and output features and respective ranges for which the model is trained. The comparison

between the predicted and experimental stress 'σ_z', 'σ_x', and 'σ_y' values revealed good harmony between them as shown in Figure 18. The models' accuracy measures are compared for the proposed three stress 'σ_z', 'σ_x', and 'σ_y' prediction models and demonstrated in Figure 19. All three ML models exhibited excellent prediction performance as reflected by evaluation metrics. Thus, the developed ML models could be implemented on sonic logs for the estimation of field stress.

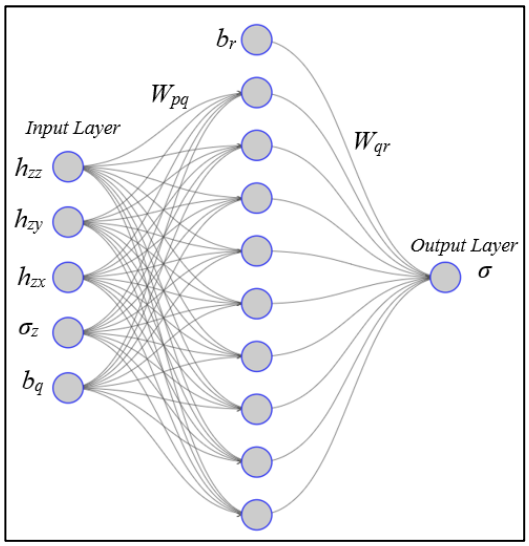

Figure 15: Generalized ANN topology showing neurons structure for stress prediction models.

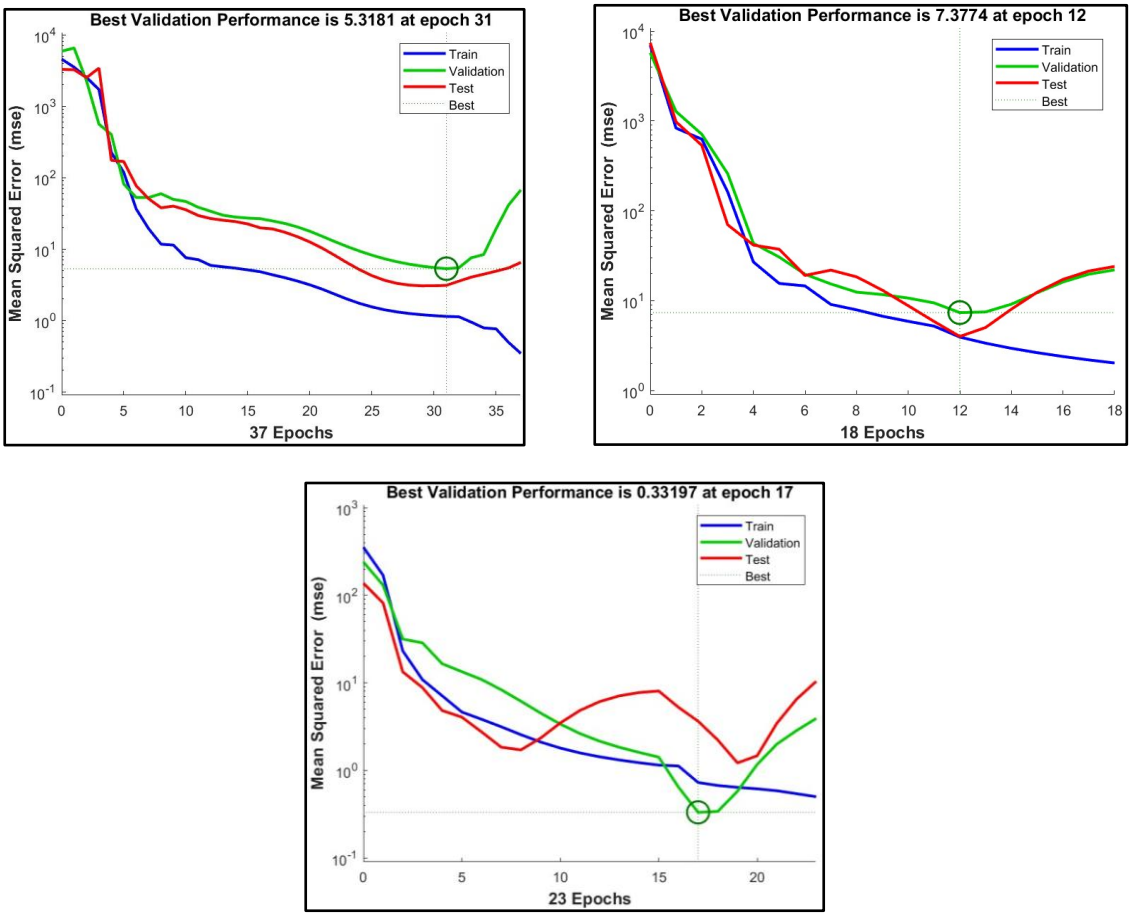

Figure 16: Models' performance during execution at optimum setting.

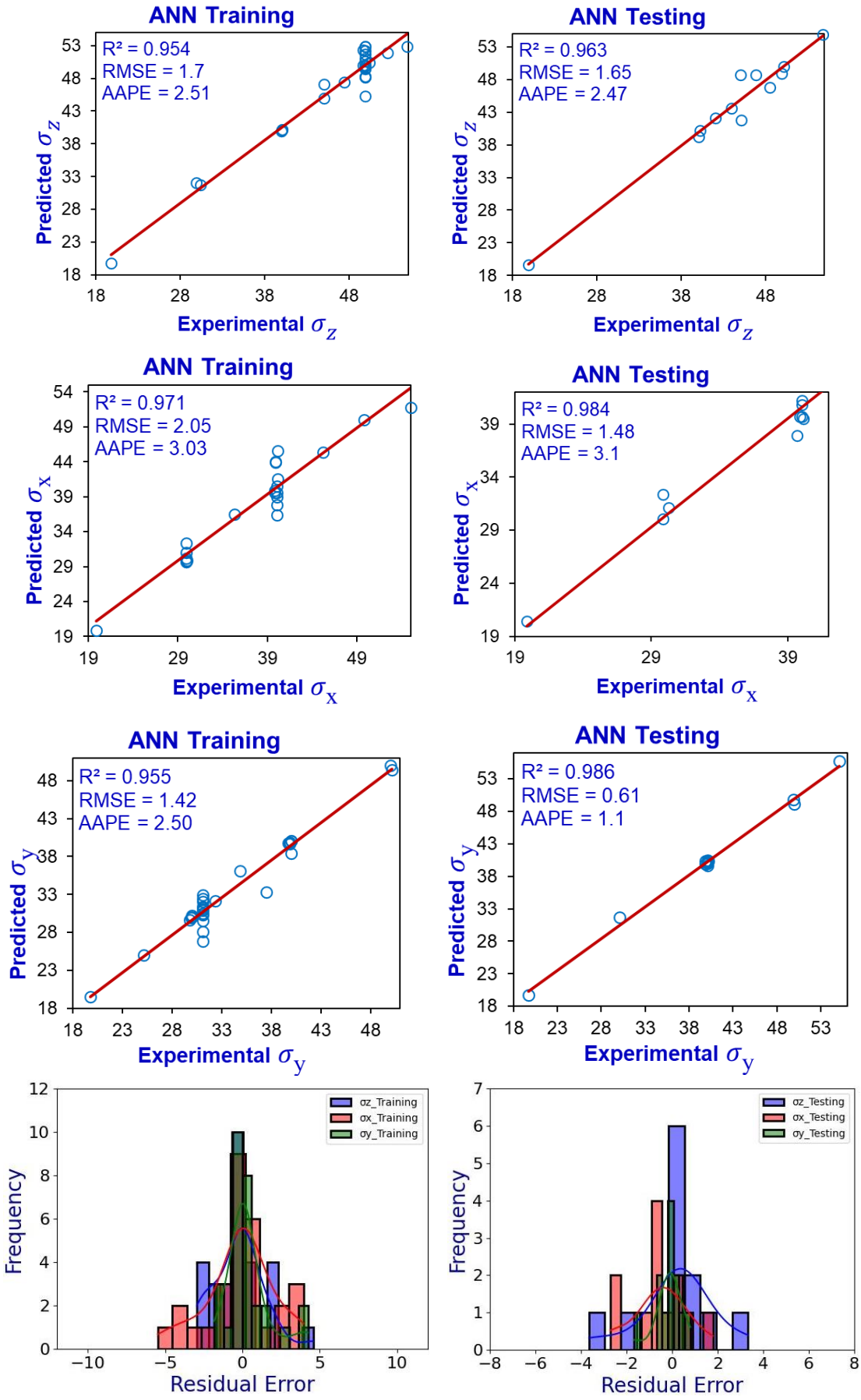

Figure 17: Training and testing prediction performance for 'σ_z', 'σ_x', and 'σ_y' for the proposed FFNN models. The last two plots represent residual error for training and testing of models.

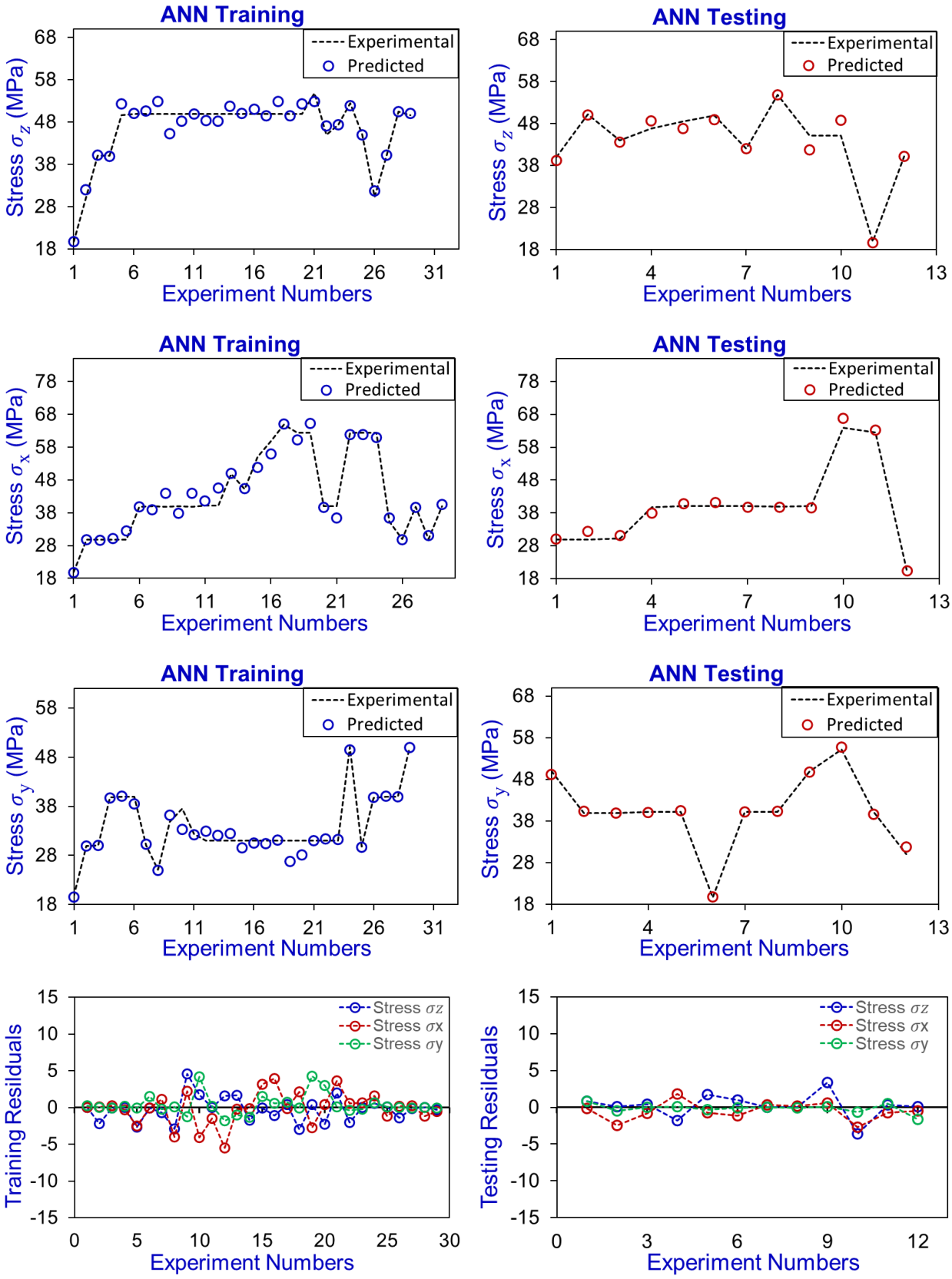

Figure 18: Comparison of testing and training predictions with experimental stresses 'σ_z', 'σ_x', and 'σ_y'. The last two plots are depicting the residual errors for training and testing outcomes.

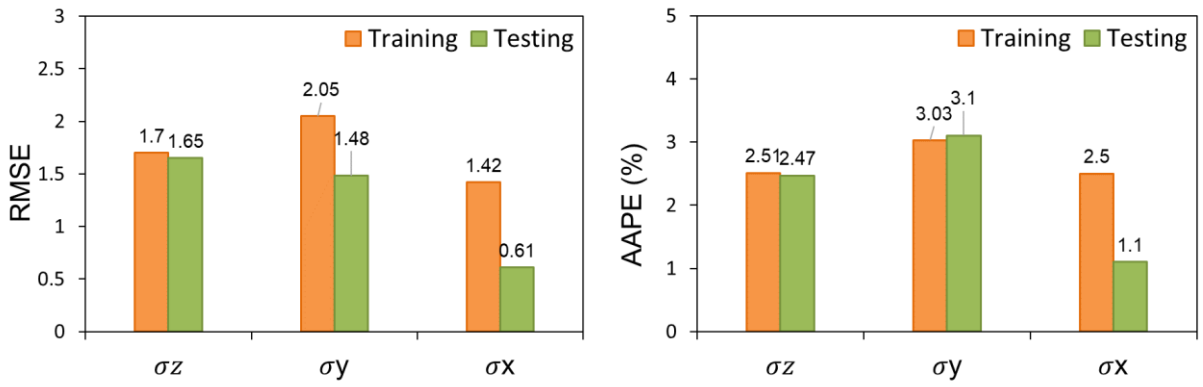

Figure 19: Comparison of prediction error RMSE and AAPE for stress 'σ_z', 'σ_x', and 'σ_y' stresses models.

6. Sensitivity Analysis (Model Generalization)

After optimizing the models' performances, it is important to evaluate whether the model has captured the underlying physics of the predicted phenomenon. Sensitivity (trend) analysis was performed to evaluate the reliability of the proposed FFNN prediction. The analysis was performed on a generated dataset in which one input feature value was changing while all other input features were kept constant. The proposed FFNN model was applied on the dataset to see the impact of changing the values of only one feature on the predicted output. Sensitivity analysis revealed that each input feature is able to uncover the underlying physics of the prediction problem effectively. The impact of each input feature such as 'h_{zz}', 'h_{zx}', and 'h_{zy}' on the predicted output was evaluated. While evaluating effects of changing P-wave slowness 'h_{zz}' on stress 'σ_z', other two S-wave slowness 'h_{zx}', and 'h_{zy}' were kept constant. The effect of 'h_{zz}' was evaluated for different combinations of 'h_{zx}', and 'h_{zy}' values as demonstrated in Figure 20. For each combination, 'h_{zz}' is following the specific trend reflecting the underlying physics of the prediction phenomenon. A similar approach was applied for evaluating the impact of S-wave slowness on the stress 'σ_z'. The results are illustrated in Figure 20.

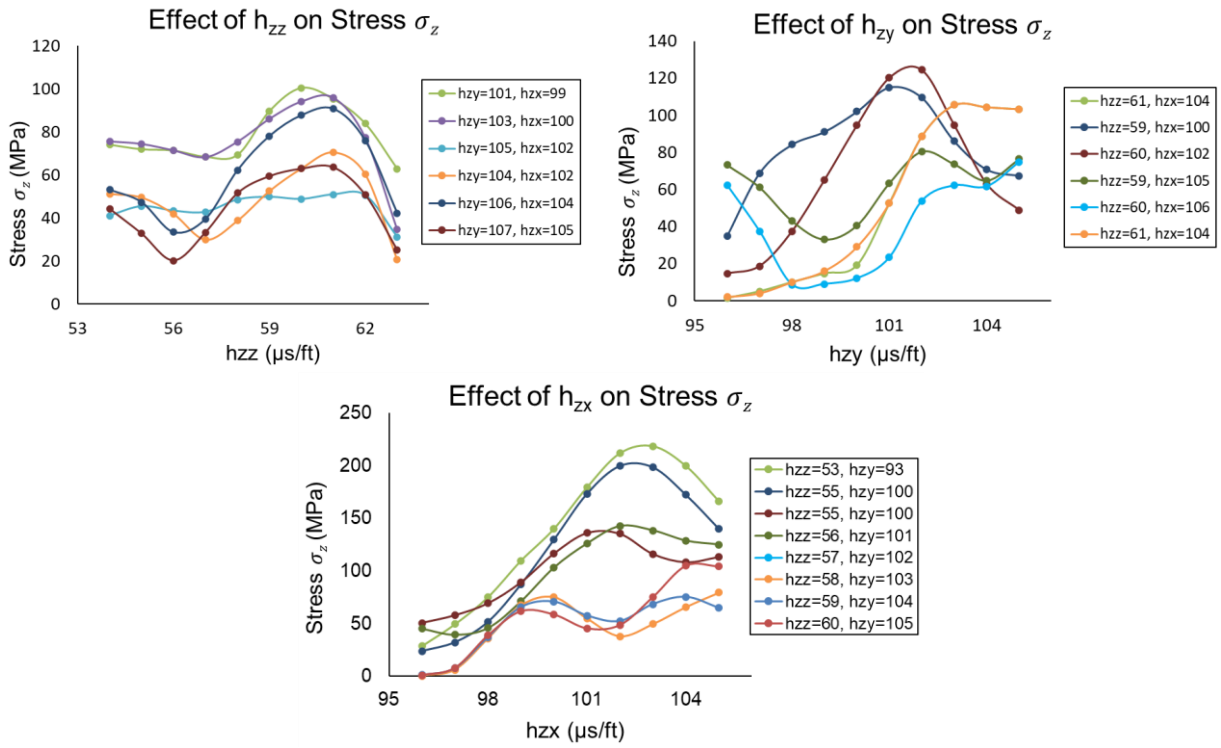

Figure 20: Sensitivity analysis results for stress 'σ_z' prediction model.

7. Stress Estimation from Well logs using Trained ML Models

The optimized setting of the FFNN model including neural network arrangements and other related hyperparameters were saved. The trained FFNN models were then implemented on field sonic log data for stress estimation in well 16A(78)-32. Sonic log data contain the vertically propagating compression wave slowness and shear wave slowness polarized in two orthogonal orientations. As mentioned in a previous section the ML models were trained on the labTUV dataset generated on Granitoid rock samples retrieved from a depth of 5474 and 5850 ft. Therefore, well log intervals ranging from 5000 to 6000 ft were selected for the in-situ stress estimation.

However, it is important to emphasize that ML based predictive models should be implemented only if the dataset contains the same statistical range of input and output features for which the models were originally trained. Therefore, the well log data underwent cleaning to bring the data within the same range of input and output features so that best prediction results could be achieved. After data cleaning, FFNN models were employed to predict vertical (S_v), minimum horizontal (Sh_{min}), and maximum horizontal (Sh_{max}) stresses using the same input features for which the models were trained.

All three FFNN trained models successfully predict the in-situ stresses for the selected log interval. The FFNN based predicted stresses using sonic logs were also compared with the field estimations of stresses that revealed good harmony between them. Specifically, the models demonstrated excellent performance for sampling depths in terms of low prediction AAPE and RMSE. Comparison between FFNN predicted and field estimations of S_v, Sh_{min}, and Sh_{max} stresses are shown in Figures 21-23, respectively.

Further, ML-based stress gradients were computed and compared with field estimations. Field estimations of vertical stress were obtained by integrating the densities of rock formations. Therefore, field estimation of S_v might be quite reliable to compare and check the consistency of ML-based in-situ stresses. However, the scenario is different for horizontal stresses that are computed using the elastic model assuming the rock is isotropic (Blanton and Olson, 1999). The stress model for the transversely isotropic

(TI) rocks is elaborated in Thiercelin and Plumb, (1994) and Higgins et al. (2008).

$$\sigma_h - \alpha\sigma_{pp} = \frac{E_{horz}}{E_{vert}} \frac{\upsilon_{vert}}{1-\upsilon_{horz}} \left(\sigma_v - \alpha(1-\xi)\sigma_{pp}\right) + \frac{E_{horz}}{1-(\upsilon_{horz})^2}\varepsilon_h + \frac{E_{horz}\,\upsilon_{horz}}{1-(\upsilon_{horz})^2}\varepsilon_H \quad \text{(Eq. 9)}$$

$$\sigma_H - \alpha\sigma_{pp} = \frac{E_{horz}}{E_{vert}} \frac{\upsilon_{vert}}{1-\upsilon_{horz}} \left(\sigma_v - \alpha(1-\xi)\sigma_{pp}\right) + \frac{E_{horz}}{1-(\upsilon_{horz})^2}\varepsilon_H + \frac{E_{horz}\,\upsilon_{horz}}{1-(\upsilon_{horz})^2}\varepsilon_h \quad \text{(Eq. 10)}$$

An elastic model approach is used to obtain the log-based horizontal stresses for TI anisotropic rocks as illustrated in Eqs. 9 and 10. The tectonic strain factors are sometimes assumed for the given basin that may lead to several uncertainties in the horizontal stress computation. Since log based Sh_{min} and Sh_{max} estimation may have been based on few assumptions it may cause a deviation from the actual stresses present at the site.

Based on this scenario, comparing ML predicted Sh_{min} and Sh_{max} with log-based Sh_{min} and Sh_{max} might not be enough to reach the firm conclusion about the consistency and reliability of the ML-based horizontal stresses (Sh_{min} and Sh_{max}). The horizontal stresses may not be taken as a benchmark for the purpose of validation of ML-based Sh_{min} and Sh_{max}.

FFNN predicted stress gradients were found to be in good agreement with the field estimations with some exceptions due to different rock types and physical properties (Figure 24). The stress gradients for S_v, Sh_{min}, and Sh_{max} stresses are demonstrated in Figure 25. A comparison revealed that FFNN intelligent models were able to capture the sonic waves variation to ultimately predict the vertical, minimum horizontal, and maximum horizontal stresses in well 16A(78)-32. The results imply that trained models and extracted mathematical correlations could be implemented to estimate the in-situ stresses.

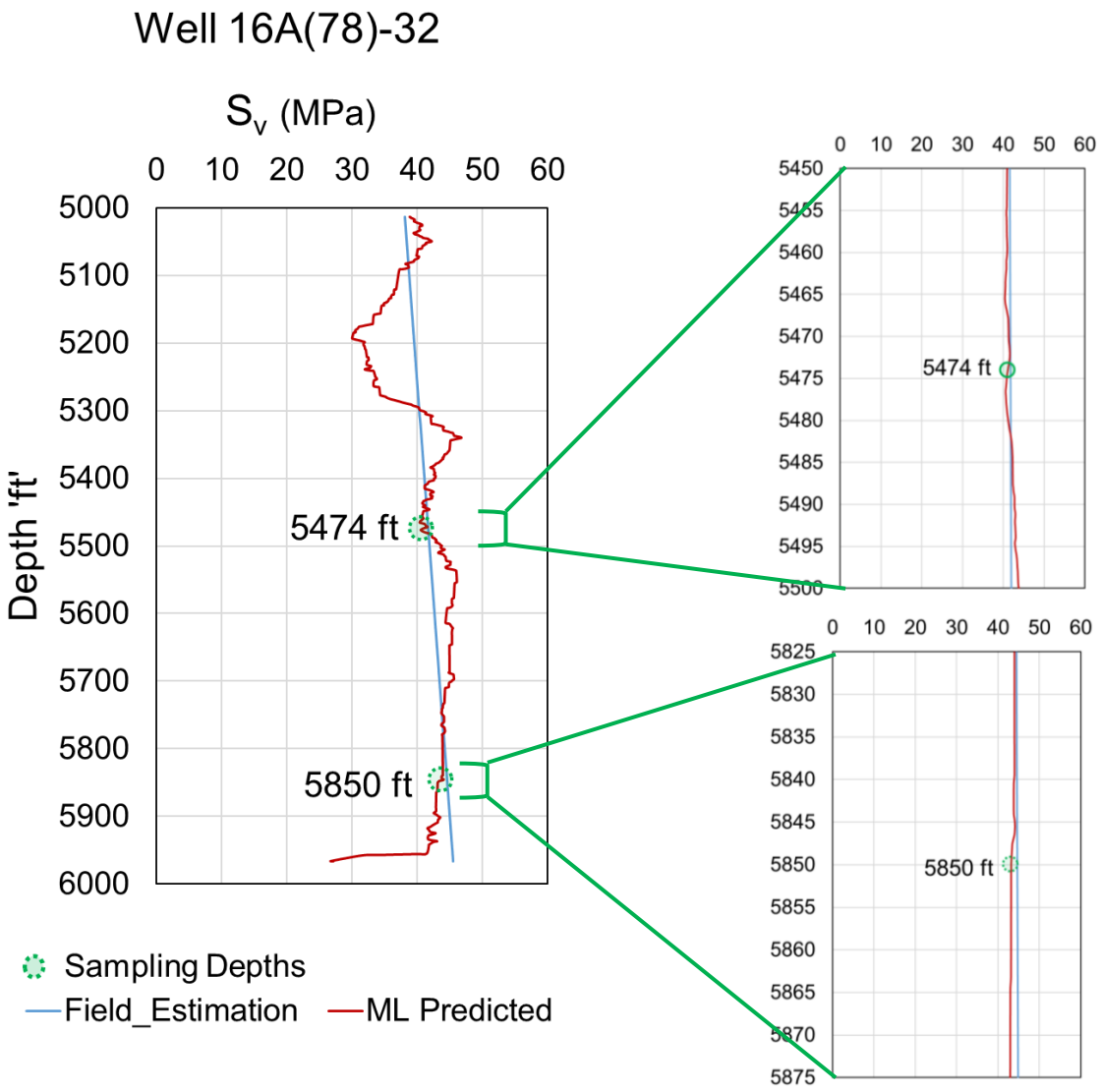

Figure 21: Vertical stress (S_v) prediction in the well 16A(78)-32 using trained FFNN model.

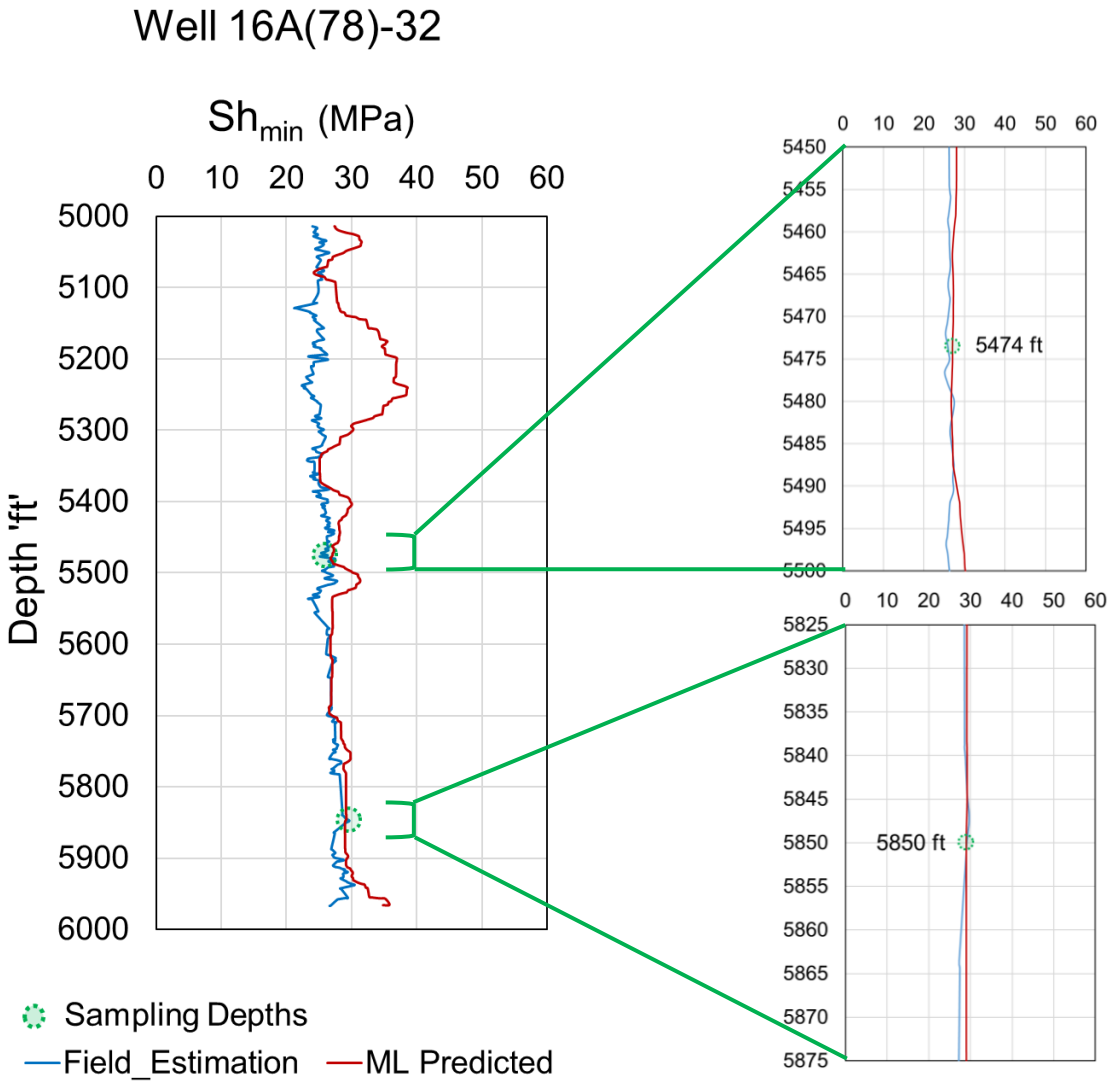

Figure 22: Minimum horizontal stress prediction in the well 16A(78)-32 using trained FFNN model.

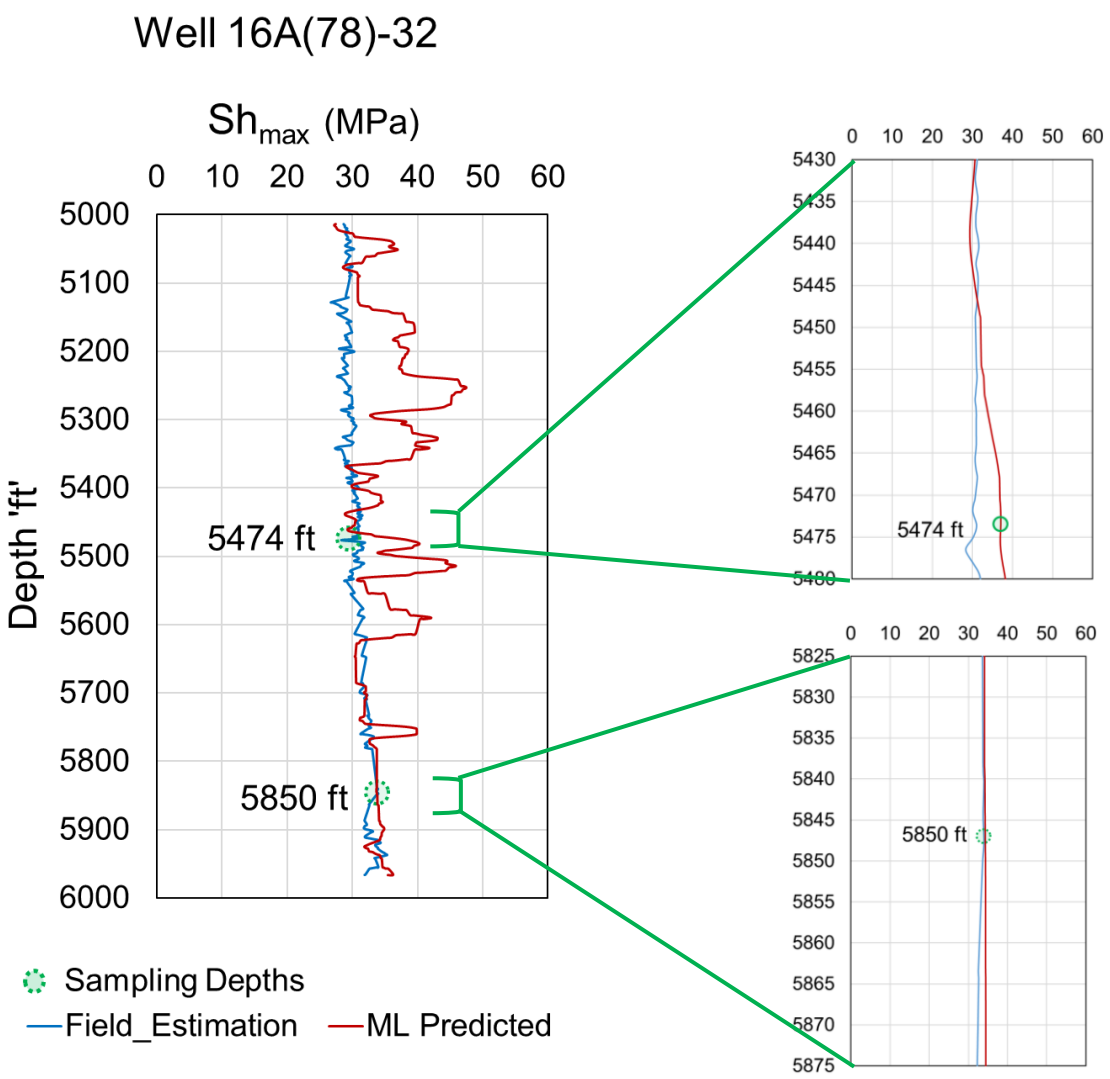

Figure 23: Maximum horizontal stress prediction in the well 16A(78)-32 using trained FFNN model.

The implementation of the FFNN model on field sonic logs for in-situ stress estimation provided a close match between field estimation and ML-based predicted in-situ stresses at the sampling depths of 5474 and 5850 feet. Further, the Granitoid rock intervals have been identified through the correlation of gamma ray and sonic logs as well as dynamic Poisson's ratio. The interval was selected based on distinctive gamma ray log value corresponding to sampling depths. It was observed that for the interval of Granitoid formation, the predicted stresses demonstrated pretty good agreement with the field estimation of stresses (Figure 23).

The stress gradients were also computed from the predicted in-situ stresses and compared with the field estimations. At the sampling depths, the FFNN predicted stresses are pretty close to field estimation. A comparison between the FFNN prediction-based stress gradients and field estimation is exhibited in Figure 24. A comparison of prediction errors for RMSE and AAPE are demonstrated in Figure 25.

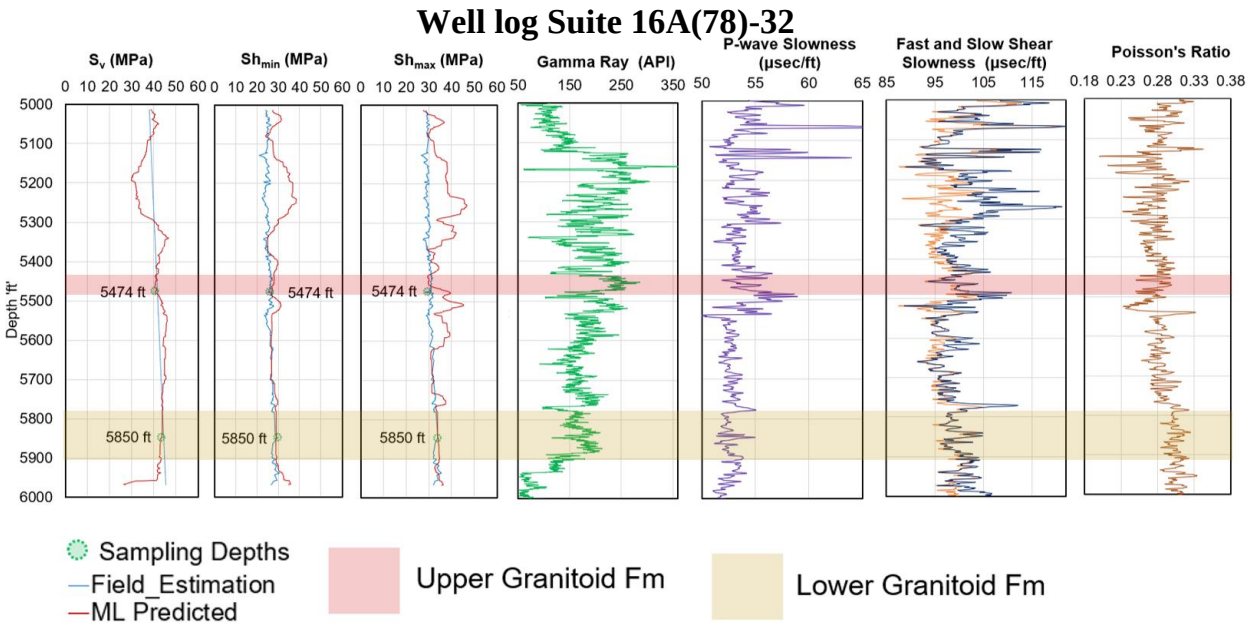

Figure 24: Correlation of in-situ stresses and well logs.

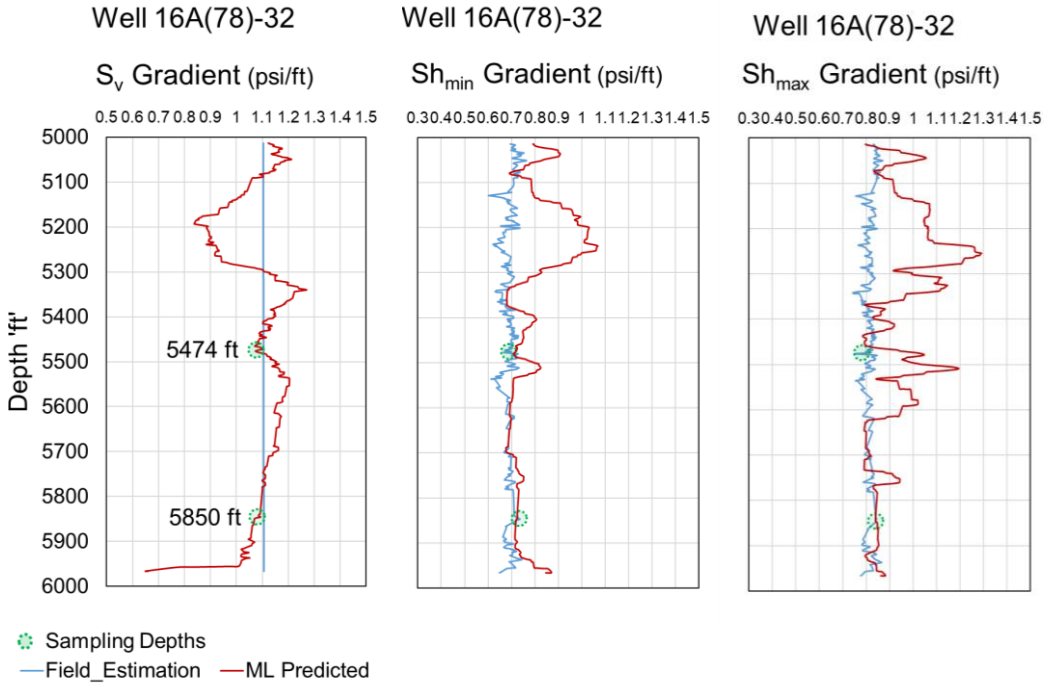

Figure 25: Comparison of ML based prediction of in-situ stress gradients and field estimation stress gradients.

8. Mathematical Correlation Development

All three optimized FFNN prediction models were converted into empirical mathematical correlations for stress estimations in vertical and two horizontal directions. The mathematical model can be conveniently used for stress estimation without running ML codes. The mathematical correlation functions well with the extracted weights and biases of an optimized FFNN model. Weights and biases for each optimized model are provided in Tables 3 through 5.

8.1. Vertical Stress 'σ_z' Prediction Model

The mathematical expression of ML prediction model is given as below.

$$(\sigma_z)_N = \sum_{q=1}^{H_n} W_{qr} n_{hq} + b_r \quad \text{(Eq. 11)}$$

$$n_{hq} = f(\sum_{p=1}^{N_p} W_{pq} i_p + b_q) \quad \text{(Eq. 12)}$$

$$n_{hq} = f\left((W_{1q}(h_{zz})_N + W_{2q}\left(h_{zy}\right)_N + W_{3q}(h_{zx})_N + b_q\right) \quad \text{(Eq. 13)}$$

$f(x) = \frac{2}{1+e^{-2x}} - 1 = \tanh(x)$ (Hyperbolic Tangent Sigmoidal Activation Function) (Eq. 14)

$$Inputs\ (i_p) = \frac{(\psi_{max}-\psi_{min})(i-i_{min})}{(i_{max}-i_{min})} + \psi_{min} \quad \text{(Eq. 15)}$$

However, input features were normalized before the FFNN simulations (using Eq. 15), where, ψ_{max} and ψ_{min} are 1 and -1 respectively. The maximum and minimum values of input features are provided in Table 1.

$$(h_{zz})_N = 0.113\left((h_{zz}) - 53.0\right) - 1 \quad \text{(Eq. 16)}$$

$$\left(h_{zy}\right)_N = 0.123\left(\left(h_{zy}\right) - 92.1\right) - 1 \quad \text{(Eq. 17)}$$

$$(h_{zx})_N = 0.182\left((h_{zx}) - 94.2\right) - 1 \quad \text{(Eq. 18)}$$

After the normalization process, input features are shown in Eqs. 16 through 18.

$$Output = \frac{(\psi_{max}-\psi_{min})(i-i_{min})}{(i_{max}-i_{min})} + \psi_{min} \quad \text{(Eq. 19)}$$

The final output values of the ML model underwent de-normalization using Eq. 19. During the de-normalization process, the values of i_{min} and i_{max} were taken as -1 and 1, respectively. ψ_{max} and ψ_{min} correspond to the maximum and minimum values of the output feature.

$$(\sigma_z) = 17.55\left((\sigma_z)_N + 1\right) - 19.8 \quad \text{(Eq. 20)}$$

The de-normalized output feature for the proposed model is shown in Eq. 20. The model biases and weights for hidden, input, and output layers of FFNN predictive model are provided in Table 3.

Table 3: Biases and weights connecting the input, output, and hidden layers for FFNN ‘σz’ models.

	Weights connecting Hidden and Input Layers (w_{pq})			**Weights between Output and Hidden Layers (w_{qr})**	**Hidden Layer Neurons bias values**
Hidden Layer Neurons (q)	Input Layer Neurons (p)			Output Neuron (r)	Bias (b_q)
	1	2	3		
1	-1.94	2.60	3.08	-0.38	5.09
2	-2.39	4.05	0.23	-0.07	4.44
3	-3.72	2.75	0.09	-0.20	4.28
4	-4.12	-2.25	1.21	0.57	3.82
5	0.49	-4.22	0.37	0.45	-4.07
6	-2.04	-3.55	2.44	-0.17	3.26
7	4.72	-0.49	-0.69	1.10	-2.85
8	-0.99	3.91	-2.44	0.18	2.88
9	-4.06	-1.71	-1.72	0.58	2.61
10	3.75	-1.82	-2.31	1.20	-2.37
11	3.95	0.61	-2.32	0.60	-2.78
12	-2.21	-4.57	-2.92	-0.61	-0.83
13	-1.47	-1.43	-3.00	-1.08	3.05
14	0.64	1.50	4.64	-1.88	-2.01
15	4.78	-3.09	-2.92	-3.02	0.16
16	-3.86	2.13	-1.56	-1.27	0.03
17	-2.11	2.01	-1.56	0.56	3.08
18	-0.22	4.58	-0.90	-3.84	-0.41
19	-4.55	-4.55	3.00	-3.62	-1.56
20	2.34	-1.68	2.58	-1.07	1.02
21	-0.49	-2.32	0.82	0.44	2.44
22	-0.26	-1.15	-5.27	-2.22	0.18
23	-3.64	2.68	-2.50	-0.95	0.55
24	-2.13	5.08	-2.59	-0.32	0.82
25	-1.53	2.69	2.43	-0.31	3.76
26	5.36	-3.66	1.96	-0.95	-1.69
27	5.01	2.18	2.60	0.75	1.39
28	-0.70	-2.58	7.00	1.19	-3.50
29	-4.82	3.30	-3.91	2.40	2.25
30	0.53	4.00	1.57	-3.49	-5.01
31	1.93	-1.74	4.89	0.50	2.27
32	-6.18	-2.84	0.79	2.65	-2.47
33	-2.43	-4.31	3.89	-2.21	-4.48
34	-0.57	4.26	-1.26	-1.16	5.15
35	-1.02	-4.40	-0.24	1.91	-2.39
36	-4.01	3.98	3.64	0.98	-4.24
37	-1.06	-3.57	1.63	-0.83	5.62
38	-2.75	-3.02	1.00	0.46	-5.46
Bias Values for Output Layer (b_r)				-0.10	

8.2. Maximum Horizontal Stress 'σ_x' Prediction Model

The mathematical expression of ML prediction model is given below.

$$(\sigma_x)_N = \sum_{q=1}^{H_n} W_{qr} n_{hq} + b_r \quad \text{(Eq. 21)}$$

$$n_{hq} = f(\sum_{p=1}^{N_p} W_{pq} i_p + b_q) \quad \text{(Eq. 22)}$$

$$n_{hq} = f\left((W_{1q}(h_{zz})_N + W_{2q}\left(h_{zy}\right)_N + W_{3q}(h_{zx})_N + W_{4q}(\sigma_z)_N + b_q\right) \quad \text{(Eq. 23)}$$

$f(x) = \frac{2}{1+e^{-2x}} - 1 = \tanh(x)$ (Hyperbolic Tangent Sigmoidal Activation Function) (Eq. 24)

$$(h_{zz})_N = 0.113\left((h_{zz}) - 53.0\right) - 1 \quad \text{(Eq. 25)}$$

$$\left(h_{zy}\right)_N = 0.123\left(\left(h_{zy}\right) - 92.1\right) - 1 \quad \text{(Eq. 26)}$$

$$(h_{zx})_N = 0.182\left((h_{zx}) - 94.2\right) - 1 \quad \text{(Eq. 27)}$$

$$(\sigma_z)_N = 0.057\left((\sigma_z) - 19.8\right) - 1 \quad \text{(Eq. 28)}$$

$$(\sigma_x) = 22.55\left((\sigma_x)_N + 1\right) - 19.9 \quad \text{(Eq. 29)}$$

The normalized input features are shown in Eq. 25 to Eq. 28. For the proposed model, the de-normalized model output is demonstrated in Eq. 29. The model biases and weights for hidden, input, and output layers of the FFNN predictive model are provided in Table 4.

Table 4: Biases and weights connecting the input, output, and hidden layers for FFNN 'σx' models.

	Weights connecting Hidden and Input Layers (w_{pq})				**Weights between Output and Hidden Layers (w_{qr})**	**Hidden Layer Neurons bias values**
Hidden Layer Neurons (q)	Input Layer Neurons (p)				Output Neuron (r)	Bias(b_q)
	1	2	3	4		
1	0.81	1.59	0.45	-2.21	-1.18	-2.58
2	1.61	0.36	-0.52	-1.51	0.66	-2.88
3	-2.25	1.18	0.99	-0.16	0.81	1.78
4	2.14	-1.67	1.05	-0.04	-0.70	-1.44
5	-1.47	-0.37	2.55	1.66	-0.42	-0.34
6	1.47	0.67	1.62	-0.12	-1.02	-0.16
7	1.22	-0.51	3.80	-2.52	2.28	-0.54
8	0.17	-3.12	1.59	-1.51	2.26	0.80
9	1.10	1.09	-2.50	0.50	1.12	-3.03
10	3.23	2.69	1.10	-1.22	-2.23	-0.37
11	-1.52	1.97	1.10	-1.44	-1.48	-1.45
12	0.57	1.14	3.96	-0.22	3.51	1.67
13	3.85	3.26	-2.90	1.02	1.60	1.75
14	0.60	-0.97	0.88	-1.59	-0.94	1.97
	Bias Values for Output Layer (b_r)				0.06	

8.3. Minimum Horizontal Stress 'σ_y' Prediction Model

The mathematical expression of ML prediction model is given below.

$$(\sigma_y)_N = \sum_{q=1}^{H_n} W_{qr} n_{hq} + b_r \quad \text{(Eq. 30)}$$

$$n_{hq} = f(\sum_{p=1}^{N_p} W_{pq} i_p + b_q) \quad \text{(Eq. 31)}$$

$$n_{hq} = f\left((W_{1q}(h_{zz})_N + W_{2q}(h_{zy})_N + W_{3q}(h_{zx})_N + W_{4q}(\sigma_z)_N + b_q\right) \quad \text{(Eq. 32)}$$

$f(x) = \frac{2}{1+e^{-2x}} - 1 = \tanh(x)$ (Hyperbolic Tangent Sigmoidal Activation Function) (Eq. 33)

$$(h_{zz})_N = 0.113\left((h_{zz}) - 53.0\right) - 1 \quad \text{(Eq. 34)}$$

$$(h_{zy})_N = 0.123\left((h_{zy}) - 92.1\right) - 1 \quad \text{(Eq. 35)}$$

$$(h_{zx})_N = 0.182\left((h_{zx}) - 94.2\right) - 1 \quad \text{(Eq. 36)}$$

$$(\sigma_z)_N = 0.057\left((\sigma_z) - 19.8\right) - 1 \quad \text{(Eq. 37)}$$

$$(\sigma_y) = 17.7\left((\sigma_y)_N + 1\right) - 19.7 \quad \text{(Eq. 38)}$$

The normalized input features are shown in Eq. 34 to Eq. 37. For the proposed model, the de-normalized model output is demonstrated in Eq. 38. The model biases and weights for hidden, input, and output layers of the FFNN predictive model are provided in Table 5.

Table 5: Biases and weights connecting the input, output, and hidden layers for FFNN 'σy' models.

	Weights connecting Hidden and Input Layers (w_{pq})				**Weights between Output and Hidden Layers (w_{qr})**	**Hidden Layer Neurons bias values**
Hidden Layer Neurons (q)	Input Layer Neurons (p)				Output Neuron	Bias(b_q)
	1	2	3	4		
1	-1.40	-1.29	0.01	1.42	-0.60	2.52
2	0.47	0.74	-3.26	0.27	-2.51	-3.11
3	-2.70	-2.36	-1.41	-0.35	2.14	1.78
4	-2.52	1.49	0.23	-1.44	-2.57	1.26
5	-0.92	-1.20	1.34	-1.80	-2.23	-0.58
6	0.10	1.75	-1.93	-2.43	2.07	0.16
7	-1.09	-3.54	0.43	-1.01	1.81	-0.73
8	2.01	1.16	-0.38	-2.03	-1.04	1.41
9	1.65	-2.19	-1.10	-2.37	-1.43	1.43
10	-0.71	1.45	2.20	-2.16	1.43	-1.95
	Bias Values for Output Layer (b_r)				-0.80	

9. Conclusions

The project Milestone comprised implementation of trained ML models (trained on labTUV) on field sonic logs for the estimation of in-situ stresses in Utah FORGE well 16A(78)-32 has been completed. In completing the milestone, labTUV-trained ML models were successfully employed for the estimation of in-situ vertical, minimum horizontal and maximum horizontal stresses. The present milestone presents the ML models as a white box which is able to capture the underlying physics of the prediction problem. The main finding of this task is that the labTUV-trained ML models are capable of estimating the in-situ vertical stress as a function of field sonic logs slowness (one P-wave and two S-waves), and horizontal stresses as a function field sonic logs slowness and vertical stress. This conclusion is developed based on promising accuracy indicators of in-situ stress prediction outcomes reflecting the reliability and robustness of the field implementation of ML models in terms of low RMSE, AAPE and high R^2. Further, ML models have uncovered the physics of the phenomenon that actually led to their successful implementation on field sonic logs for in-situ stresses prediction especially at the sampling depths. Hence, the mathematical demonstration of the proposed ML models can be employed with reasonable confidence for in-situ stress estimation across the sample zones provided that the same input/output features and ranges are used. The mathematical model has to be recalibrated if prediction is required outside of the mentioned ranges of input and output features.

Overall, the best in-situ stresses prediction performance was observed for the sampling intervals (5474 and 5850 ft) as compared to the other locations in the well. This is expected because the ML models were trained for the Granitoid samples retrieved from the same depths. Exceptions are possible at locations other than sampling depth in terms of different rock properties that lead to different sonic velocity ranges. Nonetheless, predictions of the in-situ stresses using labTUV trained ML models are of acceptable quality and provide a promising path forward for providing the economical, quick and robust solution for estimating in-situ stresses.

10.Acknowledgement

This work was performed at the University of Pittsburgh with support via Subcontract No. 845391 to Battelle Memorial Institute for Utah FORGE Project 2439, Prime Contract No. DE_EE0007080. Additional support for APB is provided by the RK Mellon Faculty Fellowship in Energy. All of these contributions are gratefully acknowledged.

11.Nomenclature

p	=	Neurons count for input layer, unitless
q	=	Neurons count for hidden layer, unitless
i_p	=	Input features after normalization, unitless
W_{pq}	=	Weight connecting input and hidden layer neurons, unitless
W_{qr}	=	Weight connecting hidden and output layer neurons, unitless
f	=	Activation function, unitless
b_r	=	bias values for output layer, unitless
b_q	=	bias values for hidden layer, unitless
N	=	Feature value after normalization, unitless
H_n	=	Total count of hidden layer neurons, unitless
N_p	=	Total count of input features, unitless
n_{hq}	=	Neuron at qth position in central hidden layer
ψ_{min}	=	Factor used to normalize the features, unitless
ψ_{max}	=	Factor used to normalize the features, unitless
h_{zz}	=	P-wave slowness in z-direction (vertical) in μsec/ft
h_{zx}	=	S-wave slowness in z-direction polarized in x-direction in μsec/ft
h_{zy}	=	S-wave slowness in z-direction polarized in y-direction in μsec/ft
$(h_{zz})_N$	=	Normalized P-wave slowness, unitless
$(h_{zx})_N$	=	Normalized S-wave slowness in z-direction polarized in x-direction, unitless
$(h_{zy})_N$	=	Normalized S-wave slowness polarized in y-direction, unitless
σ_z	=	Vertical stress in MPa
σ_x	=	1st horizontal stress (along x-direction) in MPa
σ_y	=	2nd horizontal stress (along y-direction) in MPa
$(\sigma_z)_N$	=	Normalized vertical stress output, unitless
$(\sigma_x)_N$	=	Normalized 1st horizontal stress output, unitless
$(\sigma_y)_N$	=	Normalized 2nd horizontal stress output, unitless
i	=	Input features, unitless
i_{min}	=	Input feature's minimum value, unitless
i_{max}	=	Input feature's maximum value, unitless

β_a	=	Original value, unitless
β_p	=	Predicted value, unitless
n	=	Count of data points, unitless
ΔW	=	learning components in ANN algorithm, unitless
α	=	momentum parameter, unitless
η	=	output error, unitless
E	=	adjusted weights, unitless

12.References

Ali, J.K. (1994). Neural networks: a new tool for the petroleum industry?. Society of Petroleum Engineers - European Petroleum Computer Conference, EPCC 1994. Society of Petroleum Engineers, pp. 233–242. https://doi.org/10.2523/27561-ms.

Anaconda, Inc. (2023). Anaconda distribution (Version 22.9.0). Retrieved from https://www.anaconda.com/products/distribution/

Avseth, P., Mukerji, T. (2002). Seismic lithofacies classification from well logs using statistical rock physics. Petrophysics 43, 70–81.

Blanton, T.L. and Olson, J.E. (1999). Stress magnitudes from logs: effects of tectonic strains and temperature. SPE Reservoir Eval & Eng 2 (01): 62–68. Paper Number: SPE-54653-PA

Bunger AP, Higgins J, Huang Y, Kelley M. 2023. Core-Based In-Situ Stress Estimation for Utah FORGE Well 16A(78)-32 using Triaxial Ultrasonic Velocity and Deformation Rate Analysis. Milestone Report 2.1.1 for Utah FORGE Project 2439. https://gdr.openei.org/submissions/1438

Cerezo, J., & other developers of the Spyder project. (2023). Spyder: Scientific Python Development Environment. Retrieved from https://github.com/spyder-ide/spyder

Chau, K.W. (2007). Application of a PSO-based neural network in analysis of outcomes of construction claims. Automation in construction 16 (5), 642-646.

Higgin, S., Goodwin, S., Donald, A., Bratton, T., Tracy, G. (2008). Anisotropic Stress Models Improve Completion Design in the Baxter Shale. Presented at SPE Annual Technical Conference and Exhibition, Denver, Colorado, USA. SPE 115736.

Hornik, K., Stinchcombe, M., White, H. (1989). Multilayer feedforward networks are universal approximators. Neural Network. 2, 359–366. https://doi.org/10.1016/ 0893-6080(89)90020-8.

Hunter, J. D., and Droettboom, M. (2016). Matplotlib: A 2D graphics environment. Computing in Science & Engineering, 9(3), 90-95. doi:10.1109/MCSE.2007.58

Jones, E., Oliphant, T. E., Peterson, P., and others. (2023). SciPy: Open source scientific tools for Python. Retrieved from https://scipy.org/

MATLAB User Guide, 2022. https://matlab.mathworks.com/

McKinney, W. (2022). pandas-dev/pandas: Pandas: Powerful data analysis and manipulation tool. Retrieved from https://github.com/pandas-dev/pandas

Microsoft. (2015). Visual Studio Code. [Computer software]. Retrieved from https://code.visualstudio.com/

Mohaghegh, S., Arefi, R., Ameri, S., Rose, D. (1994). Design and development of an artificial neural network for estimation of formation permeability. In: Proceedings Petroleum Computer Conference. Society of Petroleum Engineers (SPE), pp. 147–154. https://doi.org/10.2118/28237-pa.

Mozaffari, A., Azad. N.L. (2014). Optimally pruned extreme learning machine with ensemble of regularization techniques and negative correlation penalty applied to automotive engine coldstart hydrocarbon. Neurocomputing 131, 143-156.

Opper, M., & Haussler, D. (1996). Neural networks: Foundations of machine learning. Boston, MA: MIT Press.

Otchere, D.A., Ganat, T.O.A., Gholami, R., Ridha, S. (2021). Application of supervised machine learning paradigms in the prediction of petroleum reservoir properties: Comparative analysis of ANN and SVM models. J. of Pet. Sci. and Eng. Vol. 200, 108182.

Pedregosa, F., Varoquaux, G., Gramfort, A., Michel, V., Thirion, B., Grisel, O., ... & Vanderplas, J. (2011). Scikit-learn: Machine learning in Python. Journal of Machine Learning Research, 12, 2825-2830.

Python Software Foundation. (2023, May 17). Python 3.9.13. Retrieved from https://www.python.org/downloads/release/python-3913/

Saggaf, M., Toksoz, M.N., Mustafa, H.M. (2003). Estimation of reservoir properties from seismic data by smooth neural networks. Geophysics 68, 1969–1983. https://doi. org/10.1190/1.1635051

Saikia, P., Baruah, R.D., Singh, S.K., Chaudhuri, P.K. (2020). Artificial Neural Networks in the domain of reservoir characterization: A review from shallow to deep models. Computers and Geosciences, vol. 135 104357.

Thiercelin, M.J., and Plumb, R.A. (1994). Core-based prediction of lithologic stress contrasts in East Texas formations. SPE Formation Evaluation, 9 (04): 251–258. SPE-21847-PA.

Waskom, M., & Seaborn, W. (2023). seaborn: statistical data visualization. Retrieved from https://seaborn.pydata.org/

Zhang, Z., & Ye, J. (2022). On the existence of infinitely many realization functions of non-global local minima in the training of artificial neural networks with ReLU activation. arXiv preprint arXiv:2202.11481.